

## Influence of Titan's Variable Electromagnetic Environment on the Global Distribution of Energetic Neutral Atoms

Tyler Tippens<sup>1</sup> , Lucas Liuzzo<sup>2</sup> , and Sven Simon<sup>1</sup> <sup>1</sup>School of Earth and Atmospheric Sciences, Georgia Institute of Technology, Atlanta, GA, USA, <sup>2</sup>Space Sciences Laboratory, University of California, Berkeley, CA, USA**Key Points:**

- We study the effects of Titan's variable plasma interaction on the spatial distribution of the moon's energetic neutral atom (ENA) emissions
- ENA emissions form a narrow belt of high flux that is attenuated by field line draping and rotates with the inclination of the ambient field
- Outside of Titan's atmosphere, ENA detection is often non-local to production; the observable ENAs probe remote parts of the draping pattern

**Correspondence to:**T. Tippens,  
[tyler.tippens@eas.gatech.edu](mailto:tyler.tippens@eas.gatech.edu)**Citation:**Tippens, T., Liuzzo, L., & Simon, S. (2022). Influence of Titan's variable electromagnetic environment on the global distribution of energetic neutral atoms. *Journal of Geophysical Research: Space Physics*, 127, e2022JA030722. <https://doi.org/10.1029/2022JA030722>

Received 10 JUN 2022

Accepted 4 OCT 2022

**Abstract** We combine the electromagnetic fields from a hybrid plasma model with a particle tracing tool to study the spatial distribution of energetic neutral atoms (ENAs) emitted from Titan's atmosphere when the moon is exposed to different magnetospheric upstream regimes. These ENAs are generated when energetic magnetospheric ions undergo charge exchange within Titan's atmosphere. The spatial distribution of the emitted ENA flux is largely determined by the parent ions' trajectories through the draped fields in Titan's interaction region. Since images from the ENA detector aboard Cassini captured only a fraction of the ENA population, we provide context for such observations by calculating maps of the ENA flux through a spherical detector concentric with Titan. We determine the global distribution of ENA emissions and constrain deviations between the locations of ENA production and detection. We find that the ENA flux is highest in a band that encircles Titan perpendicular to the ambient magnetospheric field, which was strictly perpendicular to the moon's orbital plane during only one Cassini flyby. The field line draping strongly attenuates the emitted ENA flux, but does not alter the overall morphology of the detectable flux pattern. The majority of detectable ENAs leave Titan's atmosphere far from where they are produced, that is, even a spacecraft located directly above the moon's atmosphere would detect ENAs generated beyond its immediate environment. Some energetic parent ions produce ENAs only after they are mirrored by the field perturbations in Titan's wake and return to the moon, demonstrating the complex histories of detectable ENAs.

### 1. Introduction

In 2004 the Cassini spacecraft reached Saturn and kick-started a period of rapid expansion in our knowledge of its complex system of rings and satellites. Of particular interest has been the planet's largest moon, Titan (radius  $R_T = 2,575$  km), past which Cassini performed 126 close flybys over the course of its mission. Titan has been a point of focus in large part due to its substantial nitrogen-rich atmosphere and ionosphere. This extended neutral gas envelope plays a crucial role in the rich moon-magnetosphere interaction. Under nominal solar wind conditions, Titan orbits within the outer regions of Saturn's magnetosphere (Bertucci et al., 2009) at a distance of 20.3 Saturn radii (radius  $R_S = 60,268$  km).

As Saturn rotates faster than Titan's orbital speed and in the same direction, the moon is constantly overtaken by a stream of sub-corotating magnetospheric plasma that carries with it the magnetospheric magnetic field. The interaction of this plasma, moving with a relative velocity of around 120 km/s (Arridge, Achilleos, & Guio, 2011; Arridge, André, et al., 2011; Neubauer et al., 1984), with Titan and its ionosphere causes Saturn's magnetic field lines to strongly drape around the moon, piling up on the ramside. Newly ionized exospheric particles (primarily produced by solar EUV photoionization, see Coates et al., 2011) are picked up by the fields, creating a tail of heavy ions (primarily  $N_2^+$  and  $CH_4^+$ ) on the wakeside (e.g., Simon et al., 2015). The large pick-up ion gyroradii, up to  $10 R_T$ , cause substantial asymmetries in the plasma interaction: for a southward magnetospheric field, the tail of escaping ions is much more extended in the Saturn-averted hemisphere than in the Saturn-facing hemisphere (Luhmann, 1996; Simon, Boesswetter, et al., 2007). The region of enhanced magnetic field is thus stretched into the Saturn-averted hemisphere, along the upstream flank of the tail (Kabanovic et al., 2018; Simon, Boesswetter, et al., 2007).

Titan is subject to a diverse set of interactions with the ambient plasma, as Saturn's magnetosphere is highly dynamic near its orbit (Regoli et al., 2018). Plasma produced within the magnetosphere by the Enceladean plume experiences a centrifugal force that overwhelms gravitational and magnetic forces and drives it radially outward, carrying the planetary magnetic field with it (Gombosi et al., 2009), until it is halted by the buildup of magnetic

ension. This radial stretching results in the formation of a magnetodisk with a distinct flattened field configuration compared to a dipole field beyond about  $10 R_S$  from Saturn (Khurana et al., 2009), with strong azimuthal currents between about 8 and  $12 R_S$  (Sergis et al., 2017). Whereas a pure dipole would produce fields mainly in the north-south direction near Titan's orbital plane, the flattened geometry of the magnetodisk possesses a strong magnetic field component radial to the planet's rotation axis in the magnetodisk lobes north and south of the equatorial current sheet. In addition, the equatorial plasma sub-corotates, slowing the equatorial segment of the magnetic field lines so that their azimuthal motion lags behind that in the magnetodisk lobes to the north and south (Bertucci et al., 2009; Hill, 1979). This causes an azimuthal bulge in the magnetic field against the corotation direction, referred to as *sweepback* (Bertucci, 2009; Simon et al., 2010b). Due to this sweepback, the magnetic field has a component parallel to the corotation direction south of Saturn's magnetic equator and a component anti-parallel to the corotation direction north of it.

Titan experiences these different magnetospheric regimes across various timescales, as the moon's environment exhibits numerous non-stationarities and periodicities. High solar wind ram pressure can occasionally push back against the radial stretching of the magnetic field lines and produce a more dipolar field configuration in the dayside magnetosphere (Arridge, Russell, et al., 2008), in some cases even exposing Titan to the solar wind near noon local time (Bertucci et al., 2008, 2015; Edberg et al., 2013; Feyerabend et al., 2016). The solar wind also deforms the magnetosphere on a seasonal basis, as its flow direction is only parallel to Saturn's equatorial plane around the equinoxes (Arridge, Khurana, et al., 2008; Carbary & Mitchell, 2016). In northern summer the magnetodisk is deformed southward, exhibiting a bowl-like shape, and in southern summer it is deformed northward. This continuous (on the time scale of the Saturnian year) periodic deformation serves to push the magnetodisk current sheet away from Titan, south of the moon in northern summer and north of the moon in southern summer, for most of the Saturnian year. Superimposed are further magnetodisk oscillations in an up-and-down fashion, alternating between concave-up and concave-down as a flexible disk might if held in its center, on much smaller timescales down to 10–20 min (Arridge, Khurana, et al., 2008; Simon et al., 2010a, 2010b). As a result of all these variabilities, Titan spends much less time within the north-south aligned magnetic field near the center of the magnetodisk current sheet than within the swept-back and radially stretched fields north and south of the magnetic equator (Simon et al., 2010a, 2010b).

The sweepback of the ambient magnetic field at Titan introduces further asymmetry in the moon-plasma interaction, between the moon's northern and southern hemispheres (Simon & Motschmann, 2009). South of the magnetodisk current sheet, the upstream magnetic field is inclined in the corotation direction (i.e., toward downstream). As a result, the ramside magnetic pileup region is rotated into Titan's southern hemisphere, the maximum field strength in the pileup region is reduced, and Titan's induced magnetotail is rotated into the moon's northern hemisphere. This warping of the magnetic draping pattern occurs out to intermediate distances in the moon's wakeside hemisphere, and at larger distances ( $\geq 5 R_T$ ) the tail becomes more aligned with the corotational flow direction (Simon & Motschmann, 2009). North of the magnetodisk current sheet, the upstream magnetic field is inclined away from the corotational direction (i.e., it has a component toward upstream), and the resulting north-south asymmetries in Titan's interaction region are inverted.

Near the magnetodisk current sheet, the sub-corotating thermal plasma at Titan's orbit is dominated by singly charged oxygen (ion energy  $kT \approx 2$  keV, Arridge, Achilleos, & Guio, 2011; Arridge, André, et al., 2011). There is also an energetic (energy  $E > 10$  keV) ion population of primarily  $H^+$  and  $O^+$ , representing the high-energy tail of a Kappa distribution (e.g., Dialynas et al., 2009, 2018; Krimigis et al., 2005; Regoli et al., 2018). The energetic plasma has a number density of less than  $10^{-2} \text{ cm}^{-3}$  (Thomsen et al., 2010), several orders of magnitude lower than that of the thermal plasma, which has a number density of  $0.1\text{--}1 \text{ cm}^{-3}$  (see, e.g., Coates, 2009; Neubauer et al., 1984). While the energetic ion pressure is high near Titan (Achilleos et al., 2014; Sergis et al., 2017), numerous modeling studies have reproduced Cassini magnetometer and cold plasma observations including only the thermal ion component of the upstream flow (e.g., Feyerabend et al., 2015; Simon, Kleindienst, et al., 2007). In other words, the energetic ions were approximated as test particles that move according to a field configuration determined by Titan's interaction with the thermal population, without significantly influencing the fields themselves (Kabanovic et al., 2018; Regoli et al., 2016; Wulms et al., 2010).

An energetic ion that accesses Titan's atmosphere can undergo charge exchange with a cold neutral particle, capturing an electron from it. This produces a cold ion, which is picked up by the planetary electromagnetic fields and swept into Titan's induced magnetotail (e.g., Neubauer et al., 2006; Wahlund et al., 2005), and an

energetic neutral atom (ENA). The neutral particle is decoupled from the electromagnetic fields and travels along a straight-line trajectory from its point of origin, as gravitational forces are negligible in the keV energy range. An ENA camera, such as the *Ion and Neutral Camera* (INCA, see Mitchell et al., 1993) that was a part of the *Magnetospheric Imaging Instrument* (MIMI, see Krimigis et al., 2004) aboard Cassini, can detect these ENAs with microchannel plate sensors. INCA is sensitive to hydrogen in the 7–220 keV energy range and to oxygen in the 50–300 keV energy range. The instrument forms two-dimensional images of ENA emissions in a loosely analogous fashion to a traditional camera sensor forming an image from photons (Brandt et al., 2012; Dialynas et al., 2013; Mitchell et al., 1993). The ENA flux, integrated along the line of sight of the instrument, therefore provides remote sensing of the interaction between the thermal plasma and Titan's atmosphere. At Titan, only the ambient energetic proton population has been observed to produce sufficiently intense ENA flux for imaging (e.g., Mitchell et al., 2005).

Before Cassini arrived at Saturn, Dandouras and Amsif (1999) created an analytical model of ENA production at Titan to inform the analysis of the forthcoming INCA images. They found that the large (several  $R_T$ ) gyroradii of the energetic parent ions lead to a screening effect of Titan on the ENA emissions. The synthetic ENA images they produced are highly longitudinally asymmetric, with flux maxima and areas of depleted emissions found in opposing hemispheres as a result of the moon acting as an obstacle to certain parent ion and ENA trajectories. This screening effect causes an ENA “shadow” in the images (Dandouras & Amsif, 1999), with the areas of higher emissions forming a crescent around the moon. This crescent pattern later proved to be in qualitative agreement with images taken by INCA during the first two close Cassini flybys of Titan, TA and TB (Mitchell et al., 2005).

In their model, Dandouras and Amsif (1999) considered the circular gyromotion of parent ions in a uniform southward magnetic field and did not include the  $\vec{E} \times \vec{B}$  drift of their guiding centers. Further modeling work by Garnier et al. (2008) expanded upon this by including the  $\vec{E} \times \vec{B}$  drift motion of the energetic parent ions in constant magnetic and electric fields, showing that the “shadow” effect of the gyration is intensified under this consideration. However, neither of these models considered the effects of the highly perturbed fields near Titan on the energetic ion dynamics. Furthermore, both of them initiated parent ions everywhere around the moon, although the wake is mostly inaccessible to ions from upstream in a purely southward magnetic field due to blocking by the solid body of Titan and deflection by the perturbed fields.

Garnier et al. (2010) subsequently performed a phenomenological study of 113 INCA images from 11 flybys and confirmed that the presence of the crescent-shaped asymmetry (seen in 75% of images examined) is primarily due to the large gyroradii of the energetic parent ions. The asymmetry of Titan's pick-up tail between the Saturn-facing and Saturn-averted hemispheres was also found to be correlated with the asymmetry observed in the ENA emissions between these hemispheres. Garnier et al. (2010) showed that observed energetic parent ion and ENA fluxes were each highly variable, up to a factor of 100 and 10 difference between individual flybys, respectively. However, the mean ratio of the ENA flux to the parent ion flux ( $\approx 0.1$ ) varied only within a factor of 2 between different events. The neutral density distribution of the exosphere did not show significant variability between the events analyzed by Garnier et al. (2010). The observed variability in ENA flux between flybys is thus primarily driven by magnetospheric dynamics and not by exospheric dynamics.

Brandt et al. (2012) identified the extension of Titan's corona of exospheric hydrogen (e.g., Modolo & Chanteur, 2008) into very high altitudes (up to  $\approx 20 R_T$ ) by comparing INCA observations to modeled ENA images. These authors performed an inversion of the INCA images to determine the  $H_2$  density at high altitudes around Titan. They treated the ambient magnetospheric ion distribution as homogeneous (and thus assumed the fields to be uniform) and determined the neutral density distribution that best reproduces the observed ENA intensity. However, their modeled detector does not resolve ENA emissions at the length scales of Titan's plasma interaction ( $< 5 R_T$ ).

Wulms et al. (2010) performed numerical simulations in order to examine the influence of the draped fields on the ENA emission morphology. They compared ENA emissions in a uniform southward field and in a draped field produced by the magnetohydrodynamic (MHD) model of Backes et al. (2005) for the upstream conditions of the Cassini TA flyby. Wulms et al. (2010) showed that the draping of the fields is essential to understanding the ENA images from the TA flyby: approximating Cassini's viewing direction during TA as a plane detector at an infinite distance to Titan, they found that when field line draping is included the ENA flux maxima in their

modeled INCA images shift from the Saturn-facing to the Saturn-averted hemisphere. The magnetic enhancement in the pileup region on the ramside also reduces the accessibility of Titan's exosphere to parent ions.

Subsequently, Kabanovic et al. (2018) compared modeled ENA emissions from parent ions moving through draped fields produced by the same MHD model (Backes et al., 2005) to those produced by the hybrid model AIKEF (Feyerabend et al., 2015, 2016; Müller et al., 2011). They showed that the asymmetry in the interaction with the thermal plasma introduced by the large pick-up ion gyroradii has significant impact on the fields and must be considered in the analysis of ENA images. Compared to the MHD model, the ramside magnetic pileup region in the hybrid model is broader with a lower maximum field strength. This leads to larger parent ion gyroradii and deeper penetration of the parent ions into the ramside exosphere, increasing the intensity of ENA emissions. Kabanovic et al. (2018) also found that rotation of parent ion gyration planes in the draped fields causes an increase in ENA emissions at the poles and in the wakeside hemisphere. Conversely, the ramside pileup region in the hybrid model extends several  $R_r$  into the Saturn-averted hemisphere, deflecting parent ions that are able to access the exosphere in the MHD fields. These deflected ions no longer generate ENAs in the hybrid model, reducing the intensity of ENA emissions from this hemisphere.

ENA images contain information on the neutral gas distribution in Titan's exosphere, on the distribution of the energetic parent ions, and, because the highly perturbed electromagnetic fields near the moon strongly modify the ion distribution, on the field topology in the vicinity of the moon. ENA images can therefore be considered as global snapshots of the draped magnetic field configuration near Titan, with the "legend" needed to fully understand the information therein still, in large part, to be determined. Such a snapshot provides two-dimensional information on the moon-magnetosphere interaction as a whole, giving this method of analysis an advantage over in situ plasma and magnetic field data: observations along a spacecraft trajectory are one-dimensional and can only probe a limited portion of the induced magnetosphere during a flyby.

Previous ENA modeling studies have all considered Titan exposed to a stationary upstream magnetic field perpendicular to the orbital plane, with Wulms et al. (2010) and Kabanovic et al. (2018) also taking into account the draping of this field around Titan. However, a spacecraft is much more likely to find Titan away from these magnetospheric conditions: out of 126 flybys between 2004 and 2017 Cassini encountered Titan precisely within a steady and north-south aligned field only once, during T70 (Simon et al., 2013). The different magnetospheric regimes in which Titan is embedded significantly alter the moon-magnetosphere interaction (Regoli et al., 2018; Simon & Motschmann, 2009), but the impact of this aspect of the moon's diverse magnetic environment on its ENA emission morphology has thus far been unexplored.

In the present work, we therefore examine the influence of these upstream regimes on ENA emissions at Titan. We study the moon's ENA signature in perturbed fields for several distances between the moon and the center of Saturn's magnetodisk. We also examine ENA emissions in uniform fields to establish a "baseline." In contrast to the plane detectors used by previous ENA modeling studies, which capture only a fraction of emitted ENA flux in each synthetic image, we calculate the ENA flux into a global spherical detector. This global detector captures all detectable ENA emissions, allowing for a holistic analysis of Titan's ENA morphology without artificial truncation of emissions by the detector geometry. In this way, we study a previously largely unexplored aspect of Titan's interaction with Saturn's magnetosphere, namely the evolution of energetic ion behavior and the full distribution of associated ENA emissions in different upstream regimes of the Saturnian magnetosphere.

This paper proceeds as follows: in Section 2, we describe the constituent hybrid, test particle, and ENA production models used in this study. We also discuss the detector geometry and the layout of the global ENA maps it produces. In Section 3, we discuss the perturbed fields generated by the hybrid model and present the global ENA maps for different sweepback angles of the upstream magnetic field, as well as for uniform fields, in order to identify the influence of the field draping. In Section 4 we summarize our findings.

## 2. Model Description

In this section, we define the geometry of Titan's plasma interaction and the relevant coordinate systems (Section 2.1). We then describe the hybrid model used to calculate the electromagnetic fields near Titan (Section 2.2) and introduce the particle tracing model applied to determine the ENA emission morphology in those fields (Section 2.3). In Section 2.4 we detail the detector geometry and coordinate system used to generate the global ENA maps.

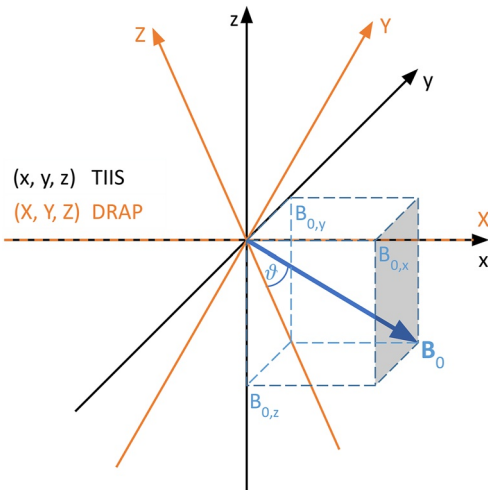


**Figure 1.** The TIIS (black) and DRAP (orange) coordinate systems, illustrated for the case of Titan in the southern lobe of Saturn's magnetodisk. Both systems are centered at Titan. In both systems, the (+x) axis points in the direction of corotation. In the TIIS, the background magnetic field generally has three non-zero components ( $\vec{B}_0 = B_{0,x}, B_{0,y}, B_{0,z}$ ). The Z axis of the DRAP system lies in the  $x = 0$  plane of the TIIS and points in direction  $(0, -B_{0,y}, -B_{0,z})$ . The Y axis completes the right-handed DRAP coordinate system. In the DRAP system, the  $B_{0,y}$  component is eliminated through rotation around the x axis and  $\vec{B}_0$  lies in the  $Y = 0$  plane. The inclination of the background magnetic field against the  $(-Z)$  axis of the DRAP system is given by the angle  $\theta$ .

## 2.1. Geometry of Titan's Magnetospheric Interaction

We first consider the Titan Interaction System (TIIS, black in Figure 1). The origin of the TIIS is at the center of Titan, the x axis points in the direction of corotation, the y axis points toward Saturn, and the z axis completes the right-handed system, that is, it is oriented northward. Due to the combined effects of the stretch and sweepback on the planetary magnetic field at Titan's orbit (see Section 1 and Simon et al., 2010b), the background field  $\vec{B}_0$  (blue in Figure 1) at the moon typically has three non-zero components: azimuthal ( $B_{0,x}$ ), radial ( $B_{0,y}$ ), and north-south ( $B_{0,z}$ ). However, the radial component caused by the centrifugal stretching can be eliminated through a rotation of the TIIS system around the x axis. In Figure 1 and throughout the text, we use capitalized labels ( $X, Y, Z$ ) to delineate this rotated system from the TIIS. Following such a rotation the background magnetic field at Titan will have only non-zero  $B_{0,z}$  and  $B_{0,x}$  components, with  $B_{0,x}$  being zero at the center of Saturn's magnetodisk current sheet, positive south of it, and negative north of it. This rotated system is called the static Draping Coordinate System (DRAP, orange in Figure 1, see e.g., Neubauer et al., 2006; Simon et al., 2013).

For example, in the southern magnetodisk lobe the magnetic field in the TIIS has a  $B_{0,y} > 0$  component pointing toward Saturn, whereas in the DRAP system, the Y axis is tilted northward and the  $B_{0,y}$  component is zero (see Figure 1). The DRAP coordinate axes are oriented differently relative to Saturn for different locations of Titan with respect to the center of the magnetodisk. The stretch of the magnetic field at these locations represents a rotation of Titan's plasma interaction around the x axis, which does not significantly alter the structure of the induced magnetosphere. Conversely, the sweepback strongly perturbs the plasma interaction due to the field

component parallel to the flow direction (Simon & Motschmann, 2009). We therefore adopt the DRAP system for this study in order to eliminate the stretch of the background field and isolate the effect of the sweepback on the induced magnetosphere and the resulting ENA morphology.

## 2.2. Titan's Electromagnetic Environment and Atmosphere

We use the same hybrid code for Titan's interaction with the thermal magnetospheric plasma as Feyerabend et al. (2015), Feyerabend et al. (2016), and Kabanovic et al. (2018), AIKEF, to calculate the perturbed fields in the vicinity of the moon. The AIKEF model treats ions as macroparticles and electrons as a massless, charge-neutralizing fluid. The kinetic treatment of the ions allows for the capture of asymmetries in the thermal plasma interaction that arise from large ionospheric pick-up ion gyroradii and flow shear between light and heavy plasma species. Because the pick-up ion gyration has a characteristic length scale comparable to the moon's radius, these factors are both critical factors in Titan's magnetospheric interaction (e.g., Feyerabend et al., 2015; Modolo & Chantaur, 2008; Modolo et al., 2007; Simon, Boesswetter, et al., 2007).

AIKEF has previously been applied to study several aspects of Titan's plasma interaction. The model has reproduced Cassini magnetometer data for flybys T9 (Simon, Kleindienst, et al., 2007) and T34 (Simon et al., 2008); has explained filamentation of the plasma density in the moon's pick-up tail seen during flybys T9, T63, and T75 (Feyerabend et al., 2015); and has reproduced both magnetic field and electron density measurements from Titan's excursion into the supersonic solar wind during the T96 flyby (Feyerabend et al., 2016). AIKEF is parallelized and runs in a hierarchical Cartesian coordinate grid. In our model runs, the simulation domain extends  $-10 R_T \leq X \leq 15 R_T$ ,  $-10 R_T \leq Y \leq 10 R_T$ , and  $-10 R_T \leq Z \leq 15 R_T$ . We use a slightly asymmetric domain with larger extensions in the +Z and +X directions to ensure the full capture of the plasma interaction in the swept-back fields of the southern magnetodisk lobe. These dimensions are sufficient for the fields to return to background values at the outer faces (see also Simon & Motschmann, 2009). We use three levels of resolution for the spatial grid:  $0.26 R_T$  for  $|X|, |Y|, |Z| > 4 R_T$ ,  $0.13 R_T$  for  $4 R_T > |X|, |Y|, |Z| > 2 R_T$  and  $0.065 R_T$  for  $|X|, |Y|, |Z| \leq 2 R_T$ . For comparison, the thermal ion gyroradii are approximately  $1.7 R_T$  (Table 1) and Titan's exospheric scale height is  $0.03\text{--}0.04 R_T$  (Cui et al., 2009). The magnetic field is initially set to the uniform background vector  $\vec{B}_0$  (see Table 1).

**Table 1**  
*Thermal Upstream Plasma Parameters for the AIKEF Simulations*

Thermal plasma parameter	Value
Magnetic field ( $B_0$ )	5 nT
Magnetic field inclination ( $\theta$ )	0°, 30°, 60°
Bulk plasma velocity ( $u_0$ )	120 km/s
Ion number density	0.14 cm <sup>-3</sup>
Ion temperature $kT$	1,500 eV
Electron temperature $kT$	200 eV
Alfvén velocity	72.9 km/s
Alfvénic Mach number	1.65
Magnetosonic Mach number	0.75
Plasma beta	3.38

Near the center of the magnetodisk the thermal plasma is dominated by singly charged atomic oxygen ( $O^+$ ), as the contribution of protons to the mass density is a factor of 16 smaller than that of the oxygen ions (Bagenal & Delamere, 2011; Neubauer et al., 1984). When Titan is far from the current sheet, however, it may be exposed to a lighter “lobe-type” plasma dominated by singly charged atomic and molecular hydrogen (Sittler et al., 2010). Such upstream conditions result in a lower plasma beta (0.51, compared to 3.38 near the current sheet). Sittler et al. (2010) found evidence of an upstream plasma dominated by light ions in the Cassini plasma spectrometer data for flybys T9 and T18. However, Kallio et al. (2007) determined through modeling of the moon-plasma interaction that an upstream plasma with both oxygen and hydrogen ions reproduces the T9 magnetometer data, while an upstream flow containing only hydrogen ions does not. There is currently no model that correlates the ambient magnetic field orientation near Titan to the thermal magnetospheric plasma composition. We therefore consider the upstream thermal plasma to contain only  $O^+$  ions in all cases.

Magnetospheric  $O^+$  temperature values observed near Titan's orbit range from below 1,000 eV (Bagenal & Delamere, 2011) through 2,000 eV (Arridge, Achilleos, & Guio, 2011; Arridge, André, et al., 2011) up to 2,900 eV (Neubauer et al., 1984). We therefore adopt the 1,500 eV value used by Kabanovic et al. (2018) as an intermediate value, yielding a plasma beta of  $\beta = 3.38$ . We also adopt the  $O^+$  upstream ion number density of 0.14 cm<sup>-3</sup> used by Kabanovic et al. (2018), which is similar to values given by Neubauer et al. (1984) and Bagenal and Delamere (2011). The magnetospheric electron temperature is set to 200 eV, consistent with the value of Neubauer et al. (1984) from Voyager data and within the third quartile of the CAPS measurements analyzed by Arridge, Achilleos, and Guio (2011) and Arridge, André, et al. (2011), see Table 6 therein. The electron temperature (or, more precisely, the electron plasma beta) enters only the electric field equation of the hybrid model. When Titan is exposed to subsonic flow, the contribution of the associated term is negligible compared to the convective and Hall terms of the electric field (Simon et al., 2006; Simon, Boeswetter, et al., 2007).

Cassini observations of the bulk plasma velocity at Titan's orbit are centered near 80 km/s (Kane et al., 2020; Thomsen et al., 2010), in line with measurements by Voyager 2 (Richardson, 1998) during a crossing of Titan's orbit that occurred far away from the moon. However, data from individual crossings of Titan's orbit cover a wide range of values. We set the upstream bulk plasma velocity in our model to  $u_0 = 120$  km/s (Hartle et al., 2006; Neubauer et al., 1984), which was measured by Voyager 1 during its flyby of Titan and falls well within the range of uncertainty in Cassini measurements (see Figure 7 in Kane et al. [2020]). In addition, this higher velocity is necessary to reproduce the magnetic field signatures measured by Cassini during multiple Titan flybys in both MHD and hybrid models (e.g., Backes et al., 2005; Feyerabend et al., 2015; Ma et al., 2006; Simon et al., 2008; Simon, Kleindienst, et al., 2007).

The sub-corotation of the plasma sheet causes the magnetic field inclination to vary with distance from the equatorial current sheet, first increasing then decreasing along the north-south direction (see Figure 4 of Simon et al., 2010b). The magnetospheric ion number density decreases with vertical distance to the plasma sheet (Bagenal & Delamere, 2011). However, while this decrease has been quantified for the inner and middle magnetosphere (Persoon et al., 2009; Thomsen et al., 2010), these empirical models do not extend beyond a radial distance of  $\approx 17R_S$ . Furthermore, variations in the upstream thermal plasma density primarily change the Alfvénic Mach number ( $M_A$ ), that is, the tilt of the Alfvén wings against the corotation direction. However, in our model the tilt of the Alfvén wings is already changed by the varying sweepback of the ambient magnetic field, even with  $M_A$  constant. Our goal is to isolate the effect of the sweepback on Titan's ENA morphology. Hence, we hold the plasma parameters constant for each background field inclination (see Table 1).

We examine three cases for  $\vec{B}_0$  with equal magnitude and varying inclination  $\vartheta$  against the  $-Z$  axis toward downstream (see Figure 1).  $\vartheta$  is defined as:

$$\vartheta = \arctan \left( \frac{|B_{0,x}|}{\sqrt{B_{0,y}^2 + B_{0,z}^2}} \right). \quad (1)$$

The sign of  $B_{0,x}$  is determined by Titan's location to either the north (negative) or south (positive) of the magnetodisk current sheet. Only positive values are included here, as a negative value for  $B_{0,x}$  would only mirror the thermal plasma interaction signatures and the ENA emission patterns across the  $Z = 0$  plane. We consider three field inclinations in this study:  $\vartheta = 0^\circ$ ,  $\vartheta = 30^\circ$ , and  $\vartheta = 60^\circ$ . The purely southward ( $\vartheta = 0^\circ$ ) case represents the field configuration at the center of the magnetodisk current sheet (as observed during T70, see Simon et al., 2013) and serves as a “baseline” to interpret the two cases with inclined upstream fields. The inclined ( $\vartheta = 30^\circ$  and  $\vartheta = 60^\circ$ ) cases represent different “strengths” of the sweepback of the ambient magnetic field. These inclinations are representative of the range of field geometries encountered by Cassini along Titan's orbit: for instance, the spacecraft measured inclinations of  $\vartheta = 30.0^\circ$  during T12 as well as  $\vartheta = 38.7^\circ$  on the inbound leg and  $\vartheta = 46.6^\circ$  on the outbound leg of T54. These values for  $\vartheta$  are calculated using Equation 1 and magnetic field vectors measured by Cassini from Simon et al. (2010b). Bertucci et al. (2009) and Wei et al. (2009) also chronicle large sweepback angles measured along Titan's orbit.

The ambient magnetospheric field magnitudes at Titan measured by Cassini show no clear correlation with the sweepback effect (Kabanovic et al., 2017; Simon et al., 2010b, 2013). For instance, during T16 and T37 the inclination was  $\vartheta = 25.0^\circ$  and  $\vartheta = 25.1^\circ$ , while Titan was exposed to a field of magnitude 6.7 and 3.9 nT, respectively. During T3 and T11 the inclination was  $\vartheta = 17.6^\circ$  and  $\vartheta = 19.4^\circ$  and the field magnitude was 4.0 and 7.1 nT, respectively. And during T4 and T8 the inclination was  $\vartheta = 26.4^\circ$  and  $\vartheta = 25.6^\circ$ , while the field magnitude was 6.0 and 3.5 nT, respectively (calculated using field vectors from Simon et al. [2010b]). This range of field magnitudes is similar across inclinations, centering around approximately 5 nT. We therefore select  $B_0 = 5$  nT as the background magnetic field strength for all cases as a reasonable intermediate value, consistent with, for example, Neubauer et al. (1984), Bertucci et al. (2009), and Simon et al. (2010a). In a 5 nT background field, the gyroradii of 30 keV protons are  $\approx 1.9 R_T$ . In 3.5 nT and 7 nT background fields (the low and high end measurements among the flybys listed previously), the gyroradii are  $\approx 2.8 R_T$  and  $\approx 1.4 R_T$ , respectively. Thus, for each of these field magnitudes the ions are able to gyrate around and avoid encountering major features of the plasma interaction, such as the magnetic pileup region as well as Titan's solid body and exosphere (Kabanovic et al., 2018; Regoli et al., 2016). As a result, the uncertainty in the choice of the upstream field magnitude does not qualitatively alter the physics embedded in our modeled ENA emission signatures.

Only the thermal upstream ion population is included in AIKEF. The energetic ion population makes non-negligible contributions to the upstream plasma's thermal pressure, with the energetic ion pressure potentially becoming dominant over the magnetic pressure at Titan's orbit (see, e.g., Achilleos et al., 2014; Sergis et al., 2017). To include any potential effects of their high pressure, energetic parent ion dynamics could in principle be calculated within the hybrid model as well. However, to achieve numerical stability the hybrid code must fulfill the Courant-Friedrichs-Lewy criterion:

$$C = \frac{u_{\max} \Delta t}{\Delta x} < 1, \quad (2)$$

where  $u_{\max}$  is the velocity of the fastest particle in the model scenario,  $\Delta t$  is the time step, and  $\Delta x$  is the local grid resolution (Müller et al., 2011). The velocity of the energetic protons ( $E > 10$  keV) is  $u_{\max} > 1,384$  km/s, that is, it is an order of magnitude greater than the thermal bulk velocity. According to Equation 2, including the energetic parent ions in the hybrid code would therefore necessitate reducing the time step by more than an order of magnitude, leading to drastically increased computing times. Despite this assumption, numerous modeling studies have successfully reproduced Cassini observations of the cold ionospheric plasma and the magnetic field without including the energetic population (e.g., Feyerabend et al., 2015; Kallio et al., 2007; Simon et al., 2008; Simon, Kleindienst, et al., 2007). Furthermore, energetic ions do not contribute appreciably to the momentum density of the plasma flow, which determines, for example, the inclination of the Alfvén wings (Neubauer, 1980).

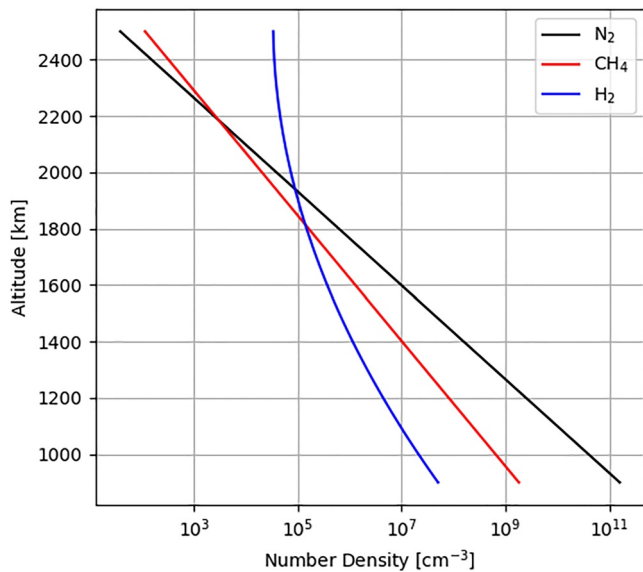


**Figure 2.** Neutral density profiles of Titan's atmosphere: altitude above the moon's surface versus particle number density for the three atmospheric species.

This suggests that the electromagnetic fields obtained from AIKEF (taking into account only the thermal ion population) are a valid approximation for use by a separate energetic particle tracing code (see Section 2.3).

In AIKEF, Titan's atmosphere is spherically symmetric and is represented by three species:  $N_2$ ,  $CH_4$ , and  $H_2$ . The number density profiles  $n_i(h)$  of these species (Figure 2) are given by barometric laws,

$$n_i(h) = n_{0,i} \exp\left(-\frac{h}{H_i}\right), \quad (3)$$

where  $h$  is the altitude above the surface,  $n_{0,i}$  is the number density at the surface, and  $H_i$  is the scale height for the respective species  $i = N_2, CH_4, H_2$ . The free parameters in Equation 3 are chosen to be consistent with Cassini Ion Neutral Mass Spectrometer (INMS) observations of Titan's atmospheric density as reported by, for example, Cui et al. (2009) using data from 15 flybys, Westlake et al. (2011) using data from 29 flybys, and Muller-Wodarg et al. (2014) taking into account data from 30 flybys. We have multiplied these observed neutral densities by a factor of 2.2 to account for subsequent revision of the INMS sensitivity model by Teolis et al. (2015). After this adjustment, the neutral profiles of nitrogen and methane in our model lie well within a standard deviation of the INMS fits presented in Westlake et al. (2011), see Figure 2 therein, and Muller-Wodarg et al. (2014), see Figures 10.6 and 10.7 therein, but are approximately a factor of 2 greater than those derived from a smaller data set by Cui et al. (2009). The hydro-

gen profile in our model is taken directly from Cui et al. (2009). For nitrogen, the surface number density and scale height in our model are, respectively,  $n_{0,N_2} = 4 \cdot 10^{16} \text{ cm}^{-3}$  and  $H_{N_2} = 72.3 \text{ km}$ . For methane, we found that  $n_{0,CH_4} = 2 \cdot 10^{13} \text{ cm}^{-3}$  and  $H_{CH_4} = 96.6 \text{ km}$  reproduce INMS observations. For hydrogen, we change these parameters at an altitude of 1,225 km:  $n_{0,H_2} = 5.82 \cdot 10^{13} \text{ cm}^{-3}$  and  $H_{H_2} = 69.8 \text{ km}$  below, and  $n_{0,H_2} = 8.52 \cdot 10^7 \text{ cm}^{-3}$  and  $H_{H_2} = 297.6 \text{ km}$  above. Above this altitude, the latter parameters better match the density curve from Cui et al. (2009) and capture Titan's high-altitude  $H_2$  corona (Modolo & Chanteur, 2008).

AIKEF includes ion-neutral collisions and a wavelength-dependent photoionization model (EUVAC, Richards et al., 1994; Feyerabend et al., 2015) to generate Titan's ionosphere from the neutral gas envelope. The ion production rate associated with ion-neutral collisions is calculated self-consistently from the local number density of the impinging magnetospheric plasma and the spherically symmetric neutral gas profile (for details, see Feyerabend et al., 2016). Solar EUV radiation is responsible for around 3.5 times more energy flux into Titan's atmosphere than ion-neutral collisions under similar upstream conditions to those in our model (Snowden & Higgins, 2021; Snowden & Yelle, 2014; Snowden et al., 2018). Therefore, AIKEF treats these collisions as elastic. For a detailed discussion, the reader is referred to Feyerabend et al. (2015). The ionosphere is primarily generated by solar EUV photoionization (Ågren et al., 2009), and thus the location of maximum ion production varies with Titan's orbital position, given by the Saturnian local time. For example, the dayside ionosphere is located on Titan's ramside at 18:00 local time and on the wakeside at 06:00 local time. However, electromagnetic field structures, including the peak magnetic field strength and morphologies of the pileup region and draping pattern, are largely independent of changes in the location of the dayside ionosphere (Ledvina et al., 2012; Simon et al., 2006; Simon, Kleindienst, et al., 2007). The electromagnetic signatures in the interaction region are rather primarily determined by the Alfvénic Mach number and the ram pressure of the upstream flow. We therefore do not expect the influence of Titan's orbital position on the electromagnetic fields to have more than a minor quantitative impact on the ENA emission morphology, and take solar UV radiation to be incident from a subsolar latitude of  $113.2^\circ$  and longitude of  $-69.0^\circ$  (the orientation of the sun during the TA flyby, local time 10:36) in all cases.

The field draping signature at Titan is not sensitive to ionospheric asymmetries as caused by, for example, the changing orientation of the moon's dayside and ramside hemispheres along its orbit around Saturn (Ledvina et al., 2012). However, a more comprehensive atmospheric profile—such as one produced by a general circulation model (GCM)—may contain asymmetries in the neutral density that could influence ENA emissions (e.g.,

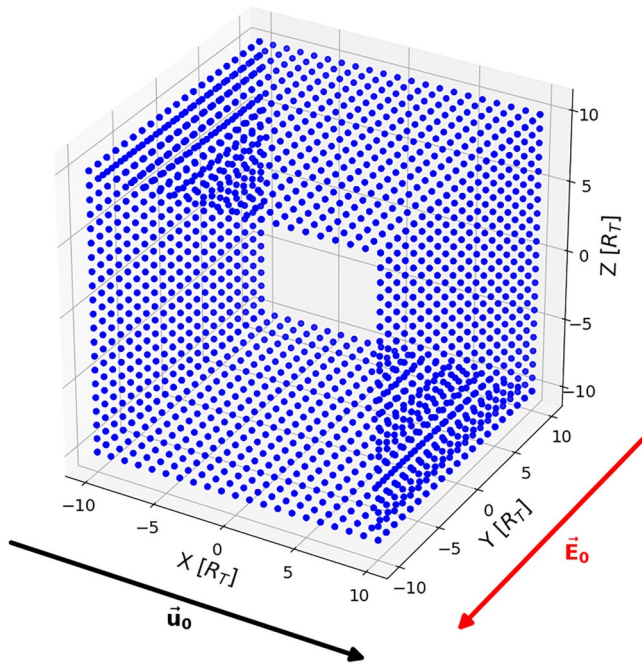


**Figure 3.** Locations where energetic parent ions are initialized in the particle tracing model. At each grid point (colored blue), 2,556 particles with energy  $E = 30$  keV are initiated to isotropically cover the surface of a sphere in velocity space. The corotational flow direction  $\vec{u}_0$  and the ambient electric field direction  $\vec{E}_0$  are indicated in black and red, respectively. The starting grid shown here has a resolution of  $1 R_T$  to make individual points visible. However, the resolution is  $0.06 R_T$  in the actual model.

Muller-Wodarg et al., 2008). Such a profile could be integrated into future ENA modeling; however, at present no GCM has produced neutral densities above around  $1,700$  km altitude (Muller-Wodarg et al., 2008). Since we simulate ENA emission up to  $2 R_T$  altitude, neutral densities above  $\approx 1,700$  km would have to be taken from another source, which may produce discontinuities in the radial density profile. These constraints make the inclusion of GCM results infeasible at present.

### 2.3. Particle Tracing and ENA Production

Similar to Wulms et al. (2010) and Kabanovic et al. (2018), we use a parallelized particle tracing model to inject high-energy parent protons into the perturbed fields produced by AIKEF and propagate them forward in time. Like AIKEF, the tracing model operates within the DRAP coordinate system, with the origin at the center of Titan. The simulation domain for particle tracing extends from  $-14 R_T \leq X \leq 14 R_T$ ,  $-14 R_T \leq Y \leq 14 R_T$ , and  $-14 R_T \leq Z \leq 14 R_T$ . Inside of the cuboid AIKEF box, the electric and magnetic fields at an arbitrary parent ion location are calculated via trilinear interpolation, using the values from the eight adjacent AIKEF grid points. Parent ions may move outside of the AIKEF box in the course of their gyration. Since the fields have returned to their background values at the edges of the AIKEF domain, the electric and magnetic fields are set to their uniform background values in this region (see Table 1).

The energetic parent ion dynamics are determined by the Lorentz force, that is,

$$\frac{d\vec{X}}{dt} = \vec{V} \quad \text{and} \quad (4)$$

$$\frac{d\vec{V}}{dt} = \frac{q}{m} (\vec{E} + \vec{V} \times \vec{B}), \quad (5)$$

where  $\vec{X}$  and  $\vec{V}$  are the particle's position and velocity,  $q$  is its charge,  $m$  is its mass,  $\vec{E}$  is the electric field, and  $\vec{B}$  is the magnetic field. The ions' motion is treated as non-relativistic, as the Lorentz factor for a 30 keV proton differs from unity by less than  $10^{-4}$ . Equations 4 and 5 are solved using the Runge-Kutta method of fourth order (RK4). The time step of integration  $\Delta t$  is adaptive: for  $|\vec{X}| > 3 R_T$ ,  $\Delta t$  is 1% of the parent ion's gyroperiod in the local magnetic field, while for  $|\vec{X}| \leq 3 R_T$  it is 0.1% of the local gyroperiod. However, to ensure the time step does not grow too large in regions where the magnetic field is weak, we establish an upper limit of either 1% or 0.1% (depending on the distance to Titan) of the ions' gyroperiod under ambient magnetospheric field conditions. The  $3 R_T$  radial threshold between the two time scales coincides with the outer boundary of Titan's atmosphere in our model. Using a smaller time step when particles are inside the atmosphere allows to better resolve the locations of ENA production. The larger time step outside of the atmosphere, where there is no ENA production, enables the simulation to run faster while still fully resolving parent ion gyration. Outside of the atmosphere, a 30 keV proton can travel no more than 50 km during one time step, less than 10% of the AIKEF grid cell size in this region. Inside the atmosphere, the same proton can travel at most 5 km in one time step, less than 4% of AIKEF grid cell size. Thus, parent ion trajectories remain well resolved even as they travel through large magnetic field gradients.

Parent ions are initiated on a Cartesian starting grid along four planes, illustrated in Figure 3: the  $X = -10 R_T$  and  $X = 10 R_T$  planes (within  $-10 R_T \leq Y \leq 10 R_T$  and  $-10 R_T \leq Z \leq 10 R_T$ ), and the  $Z = -10 R_T$  and  $Z = 10 R_T$  planes (within  $-10 R_T \leq X \leq 10 R_T$  and  $-10 R_T \leq Y \leq 10 R_T$ ). These planes are far enough from Titan that the ions are initiated in unperturbed fields (see, e.g., Kabanovic et al., 2018; Simon, Boesswetter, et al., 2007; Simon & Motschmann, 2009). The spatial resolution of the starting grid is  $0.06 R_T$ , yielding  $4 \cdot (20/0.06)^2 = 444,445$  points from which parent protons are initiated. The gyroradii of the parent ions are a factor of 33 larger than the distance between adjacent points on the starting grid. Therefore, the chosen resolution is sufficient to capture the relevant features of energetic ion dynamics near Titan.

As can be seen in Figure 3, the starting grid “wraps” around the AIKEF box (“curling” around the  $Y$  axis) to capture all points that may contain parent ions that reach Titan. Parent ions with energy  $E = 30$  keV have a velocity of  $V_0 = \sqrt{2E/m} \approx 2400$  km/s, which is much larger than the  $\vec{E} \times \vec{B}$  drift velocity. These ions can therefore have significant velocity components along the magnetic field and trajectories that are strongly inclined against the  $X$  axis. In particular, when  $\vartheta > 0$  and the upstream magnetic field is of the form  $(B_{0,X}, 0, B_{0,Z})$  with  $B_{0,X} > 0$  and  $B_{0,Z} < 0$ , that is, when Titan is located within the southern magnetodisk lobe, ions with pitch angles near  $180^\circ$  can travel antiparallel to the inclined magnetic field lines and reach Titan’s local interaction region from downstream of the moon. If the starting grid consisted of only the plane at  $X = -10 R_T$ , ions with pitch angles near  $180^\circ$  would never be able to reach Titan when the ambient magnetic field is inclined ( $\vartheta > 0$ ). We therefore initiate parent ions on both sides of the moon in the  $\pm X$  and  $\pm Z$  directions.

Ions that are launched downstream of Titan do *not* have artificially enhanced access to the atmosphere, as their  $\vec{E} \times \vec{B}$  drift velocities always have a component toward downstream, that is, along the positive  $X$  direction. In addition, the gyroradii of 30 keV protons are around  $2 R_T$ , so they cannot reach Titan from the initialization plane  $10 R_T$  downstream through gyration alone. Since the  $\vec{E} \times \vec{B}$  drift “counteracts” the precipitation of parent ions from downstream, only those particles with large velocity components antiparallel to the ambient magnetospheric field are able reach Titan from downstream. Furthermore, parent ions can reach Titan from the downstream initialization plane only if the undisturbed magnetospheric field is *not* perpendicular to the corotational flow direction (i.e., in the  $\vartheta = 30^\circ$  and  $60^\circ$  cases, but *not* in the  $\vartheta = 0^\circ$  case). We also point out that ions traveling antiparallel to the corotation direction are a common phenomenon in subsonic magnetospheric plasma flows. For instance, a drifting Maxwellian distribution in a subsonic plasma always contains a certain fraction of particles moving opposite to the bulk flow (see Figure 2 vs. Figure 8 in Khurana et al. [2008]). The reason is that in the subsonic case, the thermal velocity of the plasma (represented by the “width” of the distribution) exceeds its bulk speed.

Since the ambient magnetic field has no  $B_{0,Y}$  component (due to the rotation of the coordinate system, see Figure 1), ions that would be initiated at the  $Y = \pm 10 R_T$  planes could only reach Titan through mere gyration. Any motion along the (uniform at this distance) magnetic field lines would not bring them to smaller  $|Y|$  values, and the  $\vec{E} \times \vec{B}$  drift velocity does not have a non-zero  $V_{D,Y}$  component. However, the ions’ gyroradii are only about  $2 R_T$ , such that particles initialized on the  $Y = -10 R_T$  and  $Y = 10 R_T$  faces of the AIKEF domain can come no closer than  $6 R_T$  from Titan. Thus, we do not need to initiate particles along the  $Y = \pm 10 R_T$  planes.

An energetic ion which travels away from Titan’s local interaction region along the magnetic field lines can bounce back at a mirror point near Saturn’s polar ionosphere and return to the moon’s orbit. The gradient and curvature drifts will return the ion to Titan’s orbit with some displacement along the corotation direction ( $+X$ ). However, a full description of the guiding magnetic field lines is necessary to describe the dynamics of such bouncing ions (Roederer, 1967). Regoli et al. (2016) estimated that a bouncing 30 keV  $H^+$  ion has an azimuthal displacement of  $\approx 6 R_T$ , while its gyroradius is  $\approx 2 R_T$ . Their calculations suggest bouncing ions may return within Titan’s interaction region, which would necessitate simulating their bounce motion through the magnetosphere.

However, the estimations of the azimuthal displacement performed by Regoli et al. (2016) do not include the inherent dynamics of Saturn’s magnetodisk (which have time scales much shorter than the bounce periods, e.g., Simon et al., 2010b) and utilize a preliminary, unpublished model of Saturn’s magnetosphere from 2006 that has not been validated against observations along Titan’s orbit. While Saturn’s internal magnetic field has been well constrained for distances to the planet below  $\sim 4 R_S$ , beyond  $\sim 10 R_S$  the magnetic field is no longer dipolar and external currents dominate the magnetosphere (e.g., Arridge et al., 2007; Dougherty et al., 2018; Khurana et al., 2009). Achilleos et al. (2014) developed a “composite” model of Saturn’s magnetodisk that approximates its dynamic behavior out to Titan’s orbit by altering the geometry of a steady state magnetospheric model. However, this model has so far only been applied to Titan’s immediate environment during a single flyby (namely, T15). It does not capture the field configuration, for example, at high magnetic latitudes where a parent ion would travel during a bounce. Modeling ion bounce motion would therefore require tracing a particle along poorly constrained guiding field lines over lengths on the order of  $100 R_S$ , two orders of magnitude larger than the expected azimuthal displacements of a few Titan radii. Thus, even if the error in the calculated displacement were small on magnetospheric length scales, it would still be prohibitively large compared to the size of Titan’s local interaction region. For a realistic simulation setup, the azimuthal displacements of returning ions would have to

be calculated with an accuracy  $\ll 1 R_T$ . Therefore, a sufficiently accurate calculation of a bouncing ion's reentry point into the simulation domain is not currently feasible.

For this reason, we initialize ions on the surface of an envelope that encapsulates the entire interaction region. For instance, by initiating parent ions to ( $\pm Z$ ) of the moon, we emulate the contribution of ions returning from a bounce (with arbitrary azimuthal displacements) to the ENA emission morphology. This is similarly achieved for an inclined ambient magnetic field (i.e.,  $\theta = 30^\circ, 60^\circ$ ), where the field lines may intersect the downstream face of the simulation domain, by initiating parent ions at the ( $+X$ ) face as well. The final initialization face at ( $-X$ ) completes the envelope. In other words, our “local” approach to initialization makes it unnecessary to simulate the full bounce motion of energetic ions. Particles that return from a bounce and are about to reenter the Titan interaction region are naturally part of the ambient energetic ion distribution, as observed by Cassini and included in our model at the outer faces of the simulation domain.

At each point on the starting grid, parent ions are given an initial velocity with components

$$\begin{aligned} V_{X,0} &= V_0 \sin(\theta) \sin(\phi) \\ V_{Y,0} &= V_0 \sin(\theta) \cos(\phi) \\ V_{Z,0} &= V_0 \cos(\theta). \end{aligned} \quad (6)$$

The angles  $\theta \in [0^\circ, 180^\circ]$  and  $\phi \in [0^\circ, 360^\circ)$  define a sphere in velocity space at each node of the starting grid. Kabanovic et al. (2018) “boxed in” Titan with four plane detectors perpendicular to the  $z = 0$  plane that capture only ENAs traveling along their normal direction. These authors identified a slight dependence of the ENA emissions on the parent ion energy between 20 and 50 keV (covering most of INCA's 24–55 keV channel, see Figure 9 therein). As the ions' energies increase in this range, the ENA emission patterns captured by the model detector planes in the Saturn-averted and ramside hemispheres have their crescent shape “smeared” into a slightly more uniform ring surrounding Titan. The modeled emission patterns into the Saturn-facing and wakeside hemispheres, however, maintain their crescent shape around the moon for all energies between 20 and 50 keV. Furthermore, within this range the locations of the ENA flux maxima and minima revealed by all four plane detectors remain the same regardless of the parent ion energies. Thus, the energy dependence of the ENA emission morphology (within the range of INCA's 24–55 keV channel) is rather quantitative than qualitative. Kabanovic et al. (2018) also produced plane detector images approximating Cassini's viewing geometry during TA (see Figure 11e therein) that are integrated over the 20–50 keV parent ion energy range. Their results are consistent with those of Wulms et al. (2010), who only initialized parent ions at 30 keV (see Figure 15 therein). These results support the notion that there is no significant variation in the ENA emission pattern as the parent ion energy is increased from the lower edge to the upper edge of the 24–55 keV INCA channel. Therefore, proceeding analogous to Wulms et al. (2010) and considering a single parent ion energy far from the edges of the channel is expected to produce representative results.

We consider a monoenergetic parent ion population with  $E = 30$  keV, near the middle of INCA's sensitivity range (Mitchell et al., 1993). The resolution in velocity space is  $\Delta\theta = 5^\circ$  and  $\Delta\phi = 5^\circ$ , resulting in  $[(360/5) - 1] \cdot (180/5) = 2,556$  energetic parent ions with distinct velocity vectors launched at each point on the starting grid. A simulation run thus computes the trajectories of approximately 1.1 billion parent ion macroparticles.

At initialization, each macroparticle is assigned a numerical weight  $I_0$  describing the number of real parent ions it represents. The value of  $I_0$  was selected such that the ion flux injected at each node of the starting grid matches the 30 keV proton flux of  $\sim 100 \text{ cm}^{-2} \text{ sr}^{-1} \text{ s}^{-1} \text{ keV}^{-1}$  observed by Cassini's Low-Energy Magnetospheric Measurement System (LEMMS) and Charge-Energy-Mass-Spectrometer (CHEMS) instruments (e.g., Dialynas et al., 2009, 2018; Garnier et al., 2010; Regoli et al., 2018). Garnier et al. (2010) found the pitch angle distribution of 27–56 keV protons to be quasi-isotropic. This energy range, consisting of two LEMMS data channels, covers nearly all of the 24–55 keV INCA channel for ENA detection. We therefore assume that the pitch angle distribution outside of Titan's interaction region is isotropic. This same assumption was made by Wulms et al. (2010) and Kabanovic et al. (2018).

The minimum passing distance (MPD) is the altitude below which energetic parent ions and ENAs are thermalized by collisions with the dense neutral gas. Wulms et al. (2010) analyzed the energy-dependent stopping

powers for protons moving through Titan's atmosphere and found that ENAs which pass below 1,045 km altitude are sufficiently slowed by collisions to fall outside of INCA's 24–55 keV channel. Garnier et al. (2008) estimated the number of charge exchange collisions and resulting energy loss a parent ion experiences as it is repeatedly neutralized and re-ionized within the atmosphere. These authors determined the MPD to be located near 1,000 km and noted that a cutoff in ENA emissions around this distance is visible in low altitude INCA observations (Garnier et al., 2008). Therefore, any energetic protons or ENAs in our model that travel below the MPD are considered unobservable due to energy losses and are removed from the simulation. Establishing such a cutoff altitude at the inner boundary is consistent with both ion-neutral collision models and ENA observations (Garnier et al., 2008; Wulms et al., 2010). Furthermore, while ENAs have also been observed and modeled at greater distances to Titan than  $2 R_7$  altitude (Brandt et al., 2012), the emissions at high altitudes are at least an order of magnitude weaker than those that originate close to the exobase. This is mostly due to the exponential decay of the neutral gas density, shown in Figure 2 (see also Wulms et al., 2010). In the ion tracing model, we therefore assume that the region of ENA production has an outer boundary  $2 R_7$  from Titan's surface and an inner boundary at the MPD, 1,045 km ( $0.41 R_7$ ) above the surface.

The number density profiles for the neutral species that are used to generate ENAs in the particle tracing model are the same as those used in AIKEF (see Equation 3). However, exospheric hydrogen is not included in the ENA production process of our model. Despite  $H_2$  being more abundant than the other neutral species above approximately 2,000 km altitude, its number density is still low compared to the neutral density at lower altitudes where most ENAs are generated. At these lower altitudes,  $N_2$  and  $CH_4$  are several orders of magnitude more prevalent than  $H_2$  (see Figure 2). Hydrogen also has a charge exchange cross-section with energetic protons that is two-thirds that of nitrogen and only one-third that of methane (Janev & Reiter, 2002; Lindsay & Stebbings, 2005). This combined with its low density leads to hydrogen producing 1–2 orders of magnitude fewer ENAs, integrated across all altitudes, compared to nitrogen and methane (Amsif et al., 1997).

Parent ions that enter Titan's atmosphere undergo charge exchange with the neutral gas and produce ENAs. In our model, the neutral gas is treated as a continuum and charge exchange is described as an attenuation process for the numerical weight  $I$  of the parent ion macroparticles, an approach used previously by Wulms et al. (2010) and Kabanovic et al. (2018). During each time step that a parent ion spends within Titan's atmosphere, it loses numerical weight  $dI$  according to

$$dI = - \left( \sum_i \sigma_i n_i \right) I ds, \quad (7)$$

where  $\sigma_i$  and  $n_i = n_i(h)$  are the cross-section for charge exchange between protons and neutral density of species  $i = N_2, CH_4$ , respectively. The quantity  $ds = V dt$  is the path length of the ion's motion during the time interval  $dt$ . The sum takes into account the methane and nitrogen constituents of Titan's atmosphere. This approach allows the production of ENAs at every step along the trajectory of a parent ion macroparticle through the atmosphere. Within each time step, Equation 7 is integrated using the RK4 method. The maximum possible path length traveled by a 30 keV proton within the neutral gas during one time step  $\Delta t$  is 5 km, as determined by the upper threshold we have established for the time step in that region (0.1% of the ion's gyroperiod in the ambient magnetic field). Thus, no parent ion that produces ENAs will traverse more than approximately 7% of one atmospheric scale height during one time step. When a parent ion enters the atmosphere for the first time, the initial condition for integration is its starting numerical weight  $I_0$ , derived from Cassini observations. The cross-sections for charge exchange of  $N_2$  and  $CH_4$  with 30 keV protons are  $\sigma_{N_2} = 5.1 \cdot 10^{-16} \text{ cm}^2$  (Lindsay & Stebbings, 2005) and  $\sigma_{CH_4} = 9.1 \cdot 10^{-16} \text{ cm}^2$  (Janev & Reiter, 2002), respectively.

During each time step, the weight  $dI$  that a parent proton loses through ion-neutral interactions is transferred to a newly generated ENA macroparticle that is initiated with the ion's instantaneous position and velocity. In the keV regime, the charge exchange process involves very little energy transfer from the parent ions to the atmospheric neutral gas, on the order of  $\Delta E \approx 1 \text{ eV}$  versus parent ion energies of  $E \approx 30 \text{ keV}$  (Janev & Reiter, 2002; Lindsay & Stebbings, 2005). We therefore assume that each ENA inherits the full velocity vector of its parent ion (see also Kabanovic et al., 2018; Wulms et al., 2010). The ENAs are propagated along straight lines out to the detector (see Section 2.4), as their motion is unaffected by gravitational forces. ENAs are not detected if their trajectory passes below the MPD at any point.

Parent ions are removed from the simulation when they pass below the MPD, move beyond the outer boundaries of the particle tracing domain, or are attenuated to below 5% of their starting weight  $I_0$ . In the uniform fields outside of the AIKEF box, the direction of guiding center motion cannot change and the gyroradii are not large enough for the ion to re-encounter Titan through gyration alone. Since simulating the potential bounce motion of an escaping ion is currently infeasible (and, in our model, unnecessary), a parent ion is removed if it exits the AIKEF box with a guiding center velocity that points away from the moon.

When it enters Titan's atmosphere, the energy of a parent ion may be somewhat different from the initial value of 30 keV. However, within the energy range observable by INCA the cross-sections differ only slightly. For a hypothetical parent ion that is launched at 30 keV and accelerated to the lower or upper limits of INCA's 24–55 keV channel, the cross-sections differ from those in the 30 keV case by at most  $\approx 52\%$  (corresponding to a 55 keV ion). For comparison, the laboratory measurements used to determine the cross-sections are accurate within 15%–20% (Janev & Reiter, 2002; Lindsay & Stebbings, 2005). We emphasize that this estimation provides an upper limit for the potential change in cross-section. The acceleration encountered by energetic ions in Titan's environment is generally much smaller: selected parent ions used in our analysis possessed energies ranging from 24 to 38 keV when they produced ENAs. The cross-sections for 38 keV protons differ from those for 30 keV protons by 20%–21%, and those of 24 keV protons differ by 17%–22%. These variations are at the level of the measurement error. We therefore use the values of the cross-sections at 30 keV for all parent ions, regardless of their actual energy at a certain position.

We consider only the first neutralization of the parent ions into ENAs. Although a detected ENA may undergo multiple charge exchange collisions before leaving the atmosphere, these interactions involve little exchange of momentum and scatter the energetic particles by only small angles (Janev & Reiter, 2002; Johnson et al., 1988; Lindsay & Stebbings, 2005). As a result, we do not expect any deviations in the ENA trajectories due to subsequent collisions to substantially influence the emission morphology. Garnier et al. (2008) found that it is possible for an ENA to be ionized and complete a full gyration before subsequently being re-neutralized and detected. However, constraining the magnitude of this effect and its impact on the ENA emission morphology are beyond the scope of the present study.

## 2.4. Global ENA Mapping

Cassini's ENA camera can detect only those ENAs that travel directly toward it within its field of view. At the scale of Titan's induced magnetosphere, an instrument such as INCA can be considered point-like. In our simulation, such a detector would not encounter a sufficient number of ENAs for analysis, considering the maximum number of parent ion trajectories that can feasibly be computed (Kabanovic et al., 2018; Wulms et al., 2010). Furthermore, a spacecraft can only image a portion of the three-dimensional emission morphology for a specific set of upstream conditions. However, as the flyby-to-flyby variability in the upstream flow parameters is high at Titan (Arridge, Achilleos, & Guio, 2011; Arridge, André, et al., 2011; Simon et al., 2010b), images from multiple flybys cannot be combined to capture the ENA emission morphology in its entirety.

Previous ENA modeling studies in realistic, draped fields have utilized infinitely extended plane detectors to approximate the position of a spacecraft during imaging while still capturing enough ENAs for statistical significance (Kabanovic et al., 2018; Wulms et al., 2010). These plane detectors capture only those ENAs that strike them with velocity vectors within some angle of their normal vector, approximating a spacecraft's limited angular field of view. Such an approach is useful to emulate a single viewing position and the “filtering” of particle velocities of a spacecraft, though there are many more ENAs detected by an infinite plane than by an instrument that is point-like. This velocity filtering enables approximate comparison between modeled ENA images and actual spacecraft ENA images. However, the models of Wulms et al. (2010) and Kabanovic et al. (2018) still contain by orders of magnitude too few particles to emulate an actual, point-like detector. On the other hand, such plane detectors cannot be used to study the full global ENA population since they discard many of the ENAs generated at Titan. For instance, ENAs that move away from the plane detector or approach it at oblique angles do not contribute to the modeled image.

For this reason, the goal of our study is to examine Titan's global ENA emission morphology as a whole, without “contamination” due to our choice of viewing geometry. This approach allows for a complete picture of where ENAs can be detected and chronicles fully how the magnetospheric upstream regime maps onto the ENA

emission morphology. In contrast to all preceding studies, we therefore apply a spherical detector grid which captures every ENA that escapes Titan's atmosphere in our model, without truncation due to any particular viewing geometry. The ENA emission maps produced by a global detector (completely enveloping Titan) and ENA images taken by a point-like detector with a limited field of view (such as INCA) cannot be directly compared. The detector geometries are too different: a spacecraft detector receives ENAs along only specific velocity vectors into an approximately point-like location in the simulation domain, while the global spherical detector receives all ENAs that leave the atmosphere. Such comparisons to actual INCA images are not the goal of this study (and have already been performed by other authors, e.g., Kabanovic et al., 2018; Wulms et al., 2010). Rather, we utilize a global detector in order to comprehensively examine the influence of magnetospheric conditions on the global ENA distribution.

The spherical detector is concentric around Titan and has a radius of  $R_{\text{det}} = 3R_T$ , placing it at the top of the atmosphere (and hence, the ENA generation region) in our model. Our selection of  $3R_T$  for the radius is not critical to the ENA morphology seen in the model detector; since the ENAs move along straight lines, a larger detector will display the same emission pattern with its features somewhat "stretched" across the sphere. The detector grid has a resolution of  $3^\circ$  latitude by  $3^\circ$  longitude. We use a rotated form of the West Longitude coordinate system for the detector sphere that better aligns with the DRAP coordinates used in the hybrid and particle tracing models. In our system,  $0^\circ$  longitude is located at the (+Y) apex and longitude increases westward on the detector surface, with  $90^\circ$  downstream,  $180^\circ$  at the (-Y) apex, and  $270^\circ$  upstream. Latitude is  $90^\circ$  at the (+Z) apex,  $0^\circ$  at the detector's equator, and  $-90^\circ$  at the (-Z) apex. This coordinate system is equivalent to West Longitude coordinates that have been rotated around the X axis, such that the equator of the detector lies in the  $Z = 0$  plane of the DRAP coordinate system but does not necessarily align with Titan's geographic equator. The ENA flux  $J$  through each cell of the detector grid is defined as the sum of the numerical weights  $W_k$  of all ENAs  $k$  that pierce it, scaled by the relative size of the cell:

$$J = \frac{\sum_k W_k}{\cos \lambda}, \quad (8)$$

where  $\lambda$  is the latitude of the respective grid cell in the rotated West Longitude coordinate system.

### 3. Model Results

In this section, we first describe the important features of the electromagnetic fields produced by AIKEF for each ambient magnetospheric field orientation in Section 3.1. We then analyze the global ENA emission morphologies in uniform fields and in perturbed fields for each field orientation in Section 3.2. In Section 3.3 we identify features of the global ENA emissions that are associated with particular regions of ENA production.

#### 3.1. AIKEF Results for Titan's Electromagnetic and Cold Plasma Environment

The electromagnetic fields and  $\text{CH}_4^+$  pick-up ion densities from AIKEF are shown in Figure 4. The rows, in descending order, are the  $B_x$  component of the magnetic field, the magnetic field strength  $B$ , the number density of methane ions from Titan's ionosphere  $n_{\text{CH}_4^+}$ , and the electric field strength  $E$ . The columns correspond to different ambient magnetic field inclinations  $\vartheta$  against the (-Z) axis. Within the  $Y = 0$  plane shown here, the pick-up tails formed by ionospheric  $\text{N}_2^+$  and  $\text{H}_2^+$  look similar to those in the third row of Figure 4, though their extensions in the (-Y) direction differ due to the species' different gyroradii.

Titan's ionosphere interacts with the corotational plasma flow, slowing it, enhancing the magnetic field in the ramside hemisphere, and draping the field around the moon. While the Alfvénic Mach number is the same for all three cases, Figures 4b and 4c reveal an asymmetry between the Alfvén wings in the  $Z < 0$  and  $Z > 0$  half spaces due to the inclined background field. With increasing inclination  $\vartheta$  of the background field, the angle of the northern wing against the corotational flow direction increases and the angle of the southern wing decreases (this behavior is described analytically by Simon et al. [2022]). The strength of the  $B_x$  perturbations also becomes asymmetric due to the different Alfvén conductances in the wings when  $\vec{B}_0$  is not perpendicular to the corotation direction (Neubauer, 1980). The magnitude of the  $B_x$  perturbation is larger in the  $Z < 0$  wing than in the  $Z > 0$  one, by a factor of 1.7 in the  $\vartheta = 30^\circ$  case and 3.0 in the  $\vartheta = 60^\circ$  case. These asymmetries in our model are consistent with the modeling results of Simon and Motschmann (2009).

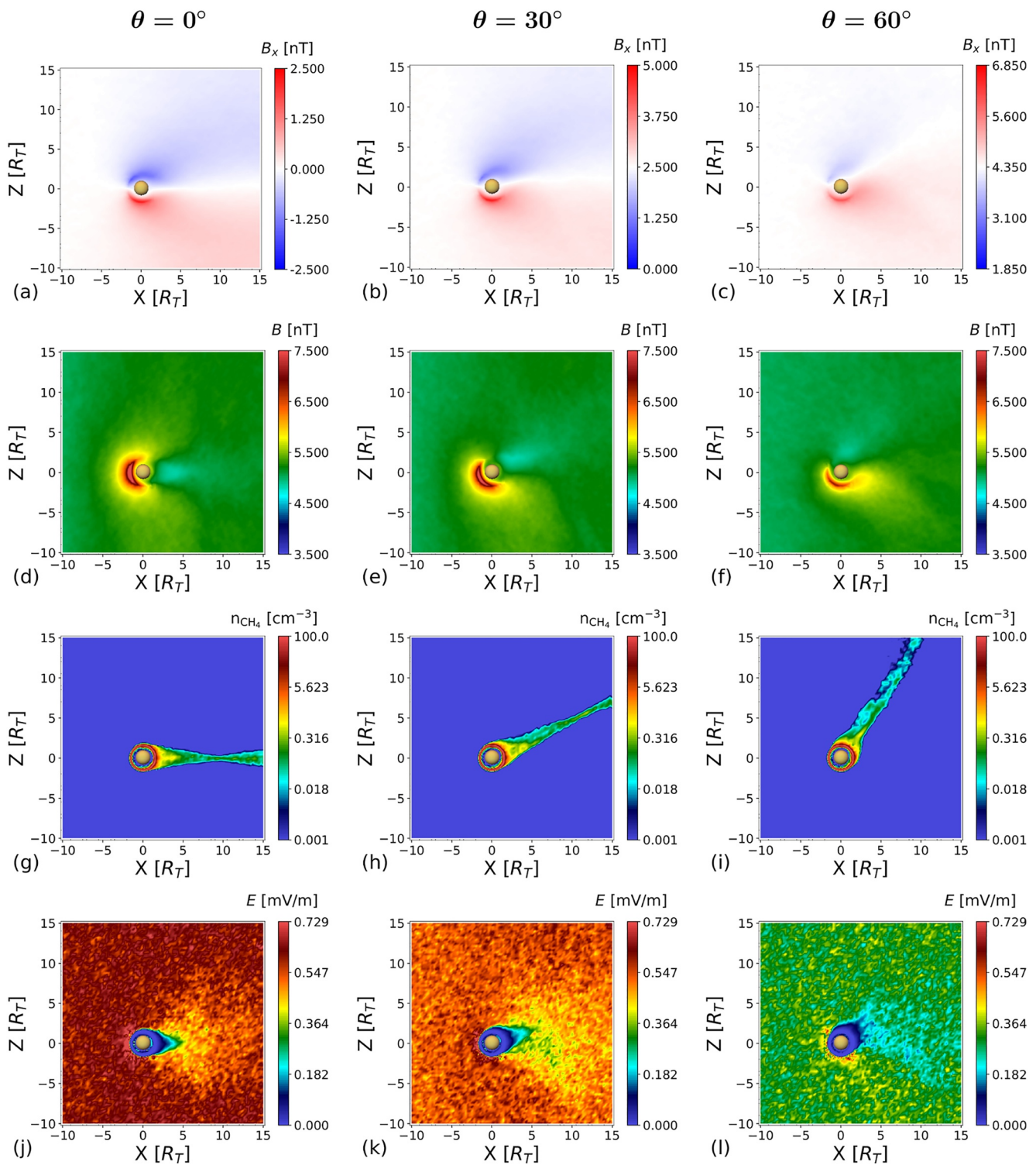


**Figure 4.** Magnetic and electric fields near Titan and methane pick-up ion number densities produced by AIKEF. Plots (a–c) show the  $B_x$  component of the magnetic field, plots (d–f) show the magnetic field magnitude, plots (g–i) show the density of ionospheric  $\text{CH}_4^+$  ions, and plots (j–l) show the electric field magnitude. All plots show the  $Y = 0$  plane, which is perpendicular to the undisturbed convective electric field  $\vec{E}_0$ . The first column has the ambient magnetic field  $\vec{B}_0$  inclined against the  $(-Z)$  axis by  $\theta = 0^\circ$ , the second column by  $\theta = 30^\circ$ , and the third column by  $\theta = 60^\circ$ .

When  $\vec{B}_0$  points southward ( $\vartheta = 0^\circ$ ), a magnetic pileup region forms upstream of Titan that is symmetric between the  $Z > 0$  and  $Z < 0$  half spaces and extends toward downstream to the  $X = 0$  plane (Figure 4d). The maximum magnetic field strength is 8.2 nT (1.6 times the background field  $B_0 = 5$  nT), within the typical range of enhancement observed in this region during Cassini flybys of Titan (Chen & Simon, 2020). For  $\vartheta = 0^\circ$ , the magnetic enhancement in the pileup region upstream begins around  $3 R_T$  altitude and peaks around  $0.65 R_T$  altitude. It starts decreasing around  $0.55 R_T$  altitude, just above the MPD ( $\approx 0.4 R_T$  altitude). The field strength at the MPD is about 85% of its peak value. The modeled shape of the pileup region is in quantitative agreement with Cassini observations. In a survey of MAG data from all 126 flybys of Titan, Chen and Simon (2020) found that, on average, magnetic enhancement in the pileup region begins around  $2.8 R_T$  altitude at the ramside, peaks between  $0.65 R_T$  (in the  $Y > 0$  hemisphere) and  $0.75 R_T$  altitude (in the  $Y < 0$  hemisphere), and weakens between  $0.35$  and  $0.45 R_T$  altitude.

When  $\vec{B}_0$  has a component along the corotation direction (Figures 4e and 4f), the pileup region is wrapped around Titan in the  $Z < 0$  half space and even penetrates into the moon's geometric plasma shadow. This stretching of the pileup region into Titan's wake occurs due to the field-aligned component of the corotational flow dragging the magnetic field lines downstream. The region where the magnetic field is enhanced by at least 15% extends farther downstream with greater inclination  $\vartheta$ , reaching  $X = 2 R_T$  downstream in the  $\vartheta = 30^\circ$  case and  $X = 3 R_T$  downstream in the  $\vartheta = 60^\circ$  case. On the ramside, the pileup region is thinner and the field enhancement weaker in the  $\vartheta \neq 0^\circ$  cases compared to the  $\vec{u}_0 \perp \vec{B}_0$  case: the ramside pileup is approximately  $3.0 R_T$  thick with a maximum field value of  $1.62 B_0$  when  $\vartheta = 0^\circ$ , approximately  $1.5 R_T$  thick with a maximum field value of  $1.54 B_0$  when  $\vartheta = 30^\circ$ , and approximately  $0.5 R_T$  thick with a maximum value of  $1.35 B_0$  when  $\vartheta = 60^\circ$ . Since the magnetic field enhancement in the pileup region acts as a partial barrier that deflects energetic parent ions, the wrapping, weakening, and downstream stretching of this region all affect energetic parent ion trajectories.

In the vicinity of Titan, the pick-up ions (Figures 4g–4i) are largely confined to the magnetic neutral region between the moon's magnetic lobes, visible in the  $Y = 0$  plane as a thin white region downstream of Titan in Figures 4a–4c and as light blue in Figures 4d–4f. This confinement mainly occurs due to the lower magnetic pressure in this region and the heavy pick-up ions' large gyroradii preventing the formation of a full ring distribution within the AIKEF domain, that is, scattering of the pitch angle distribution does not occur before the ions reach the downstream face of the AIKEF domain (see also Cowee et al., 2010). The (nearly) cycloidal arcs of the pick-up ion trajectories extend  $3\text{--}5 R_T$  out of the  $Y = 0$  plane shown in Figure 4 and into the  $Y < 0$  half space. The ramside pileup region is extended along the leading edge of the pick-up tail in this half-space (see, e.g., Figures 5 and 6 of Simon, Boesswetter, et al. [2007], Figure 3 of Feyerabend et al. [2015], and Figure 4 of Kabanovic et al. [2018]), in agreement with Cassini observations (Chen & Simon, 2020). Due to the pick-up ions' large gyroradii and confinement to the neutral region the moon's pick-up tail is effectively flat (see also Simon & Motschmann, 2009; Simon, Boesswetter, et al., 2007), such that, in the  $\vartheta = 0^\circ$  case, the tail resides in the  $Z = 0$  plane. In the  $\vartheta = 30^\circ$  and  $\vartheta = 60^\circ$  cases, however, the plane of the pick-up tail is rotated toward (+Z) by approximately the ambient field inclination angle  $\vartheta$  (see the third row of Figure 4).

The magnitude of the upstream convective electric field,  $\vec{E}_0 = -\vec{u}_0 \times \vec{B}_0$ , decreases with greater inclination of the ambient magnetic field against the ( $-Z$ ) axis: the background electric field is  $E_0 = 0.6$  mV/m in the  $\vartheta = 0^\circ$  case,  $E_0 = 0.5$  mV/m in the  $\vartheta = 30^\circ$  case, and  $E_0 = 0.3$  mV/m in the  $\vartheta = 60^\circ$  case. This decrease is visible in the different background field colors in Figures 4j–4l. Also visible in Figures 4j–4l is the reduction in the electric field downstream of the moon to  $\approx 80\%$  of the background value, due to the deflection of the upstream flow around the obstacle. In the plane of the pick-up tail, the electric field is further weakened to  $\approx 50\%$  of the background value within  $4 R_T$  of Titan. In Figures 4j–4l, this is denoted by the light and dark blue taper downstream of the moon. This additional reduction in  $E$  occurs where the slow pick-up ions are the dominant species, lowering the average plasma velocity and thus the convective electric field.

For a more detailed discussion of the electromagnetic and plasma perturbations near Titan, the reader is referred to the numerous preceding publications that are based on the same model (e.g., Feyerabend et al., 2015, 2016; Kabanovic et al., 2018; Simon & Motschmann, 2009).

### 3.2. Global Maps of the ENA Emission Morphology

Global ENA flux maps from the concentric spherical detector are shown in Figure 5. The first and second rows display the ENA fluxes in uniform electromagnetic fields and the fluxes in the perturbed fields produced by

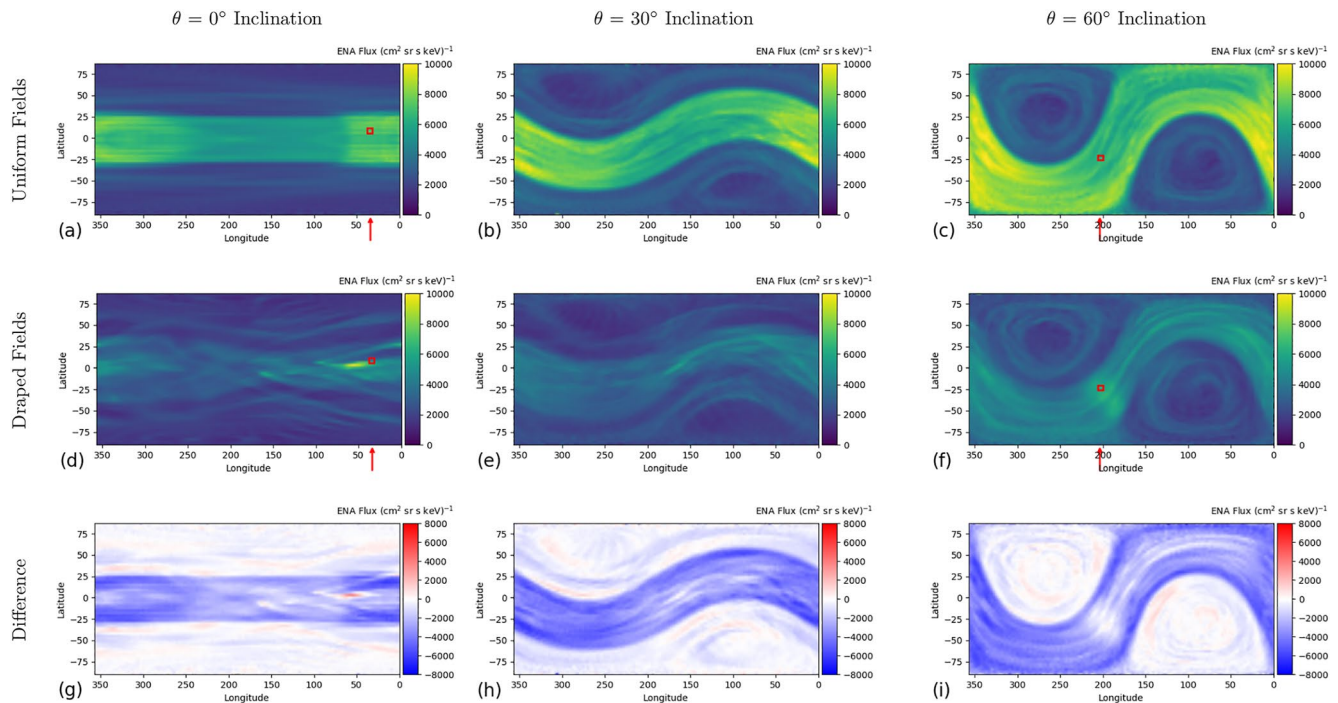


**Figure 5.** Global energetic neutral atom (ENA) flux maps produced by the ENA model. The detector is concentric around Titan with radius  $3 R_T$ . The coordinates are in the rotated West Longitude system described in Section 2.4, with the ramside apex at  $270^\circ$  W. Plots (a–c) show the ENA flux maps for uniform fields and plots (d–f) show the maps for the perturbed fields from the AIKEF hybrid model. The columns show results for the three inclinations  $\vartheta = 0^\circ, 30^\circ,$  and  $60^\circ$  of the ambient magnetic field  $B_0$  against the  $(-Z)$  axis. The red boxes pointed out by red arrows denote locations where selected ENAs emitted by the parent ion trajectories plotted in Figure 7 are detected. Plots (g–i) are difference maps of the ENA flux in uniform fields subtracted from the flux in perturbed fields, that is, the second row minus the first row. The values of this difference are shown in red where the ENA flux is stronger in the perturbed case and in blue where it is stronger in the uniform case.

AIKEF, respectively, in units of particles/( $\text{cm}^2 \text{sr s keV}$ ). The third row is the change in ENA flux between the perturbed and uniform cases. In these difference plots, the value is positive (red) where the ENA flux is higher in the perturbed case and negative (blue) where it is higher in the uniform case. The columns correspond to different ambient magnetic field inclinations  $\vartheta$  against the  $(-Z)$  axis, as in Figure 4. All plots in Figure 5 use the rotated West Longitude coordinate system described in Section 2.4.

Figure 6 gives an illustration of the effect of the ambient magnetic field inclination on the parent ions' gyroplanes and consequently on their ENA emissions. Selected parent ion trajectories that emit ENAs into regions of interest in the global ENA flux maps are shown in Figure 7. The left column of each panel shows an ion's path through uniform fields (colored orange) and the right column of each panel shows an ion's path through draped fields (colored red). The trajectories are colored green when the ions are within Titan's atmosphere above the MPD and emitting ENAs. Though many of the green arcs in all four panels appear contiguous in the projection of the trajectories onto the  $Z = 0$  plane, the projection onto the  $Y = 0$  plane illustrates that these arcs are discrete “segments” where the parent ions produce ENAs. This segmented emission occurs due to the depicted ions gyrating into and out of Titan's atmosphere multiple times before being fully attenuated, crossing the MPD, or leaving the interaction region. Along the green segments, the neutralization of individual real parent ions is represented by the attenuation of the parent ion macroparticle's numerical weight. For instance, each time the ions shown in Figure 7a gyrate into the atmosphere, they convert some of their numerical weight into ENA flux (see Equation 7) that is emitted at tangents to the green arcs of the trajectories.

The sweepback of the upstream magnetic field has a clearly discernible influence on the global ENA emission morphology. In uniform fields, the ENA flux integrated over the entire detector sphere increases by 25% when the field inclination increases from  $\vartheta = 0^\circ$ – $30^\circ$ , and by another 23% when the inclination increases from  $\vartheta = 30^\circ$ – $60^\circ$

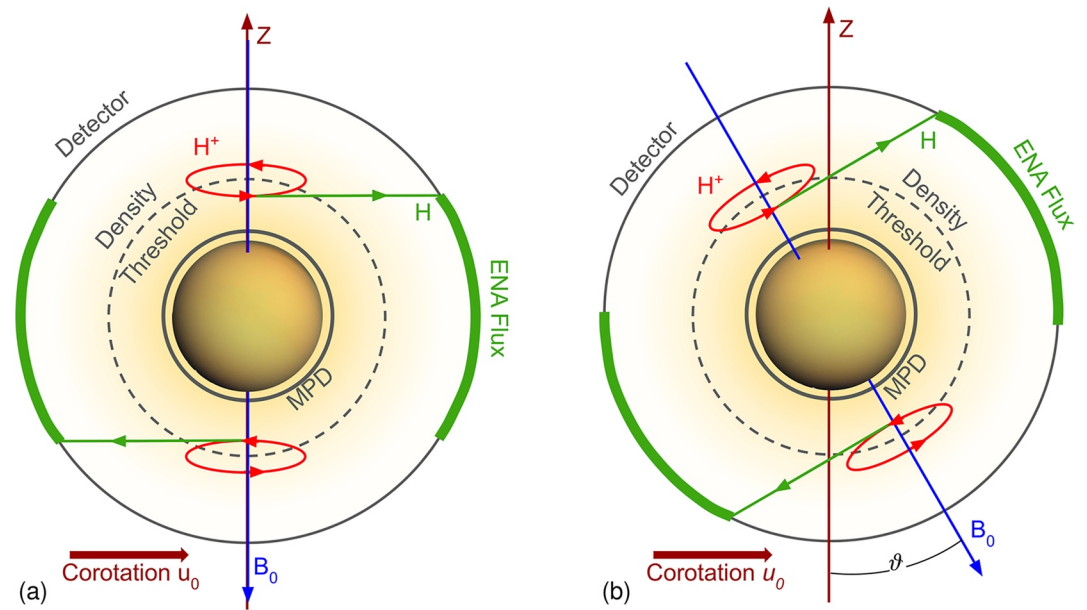


**Figure 6.** Explaining flux differences on the detector using the limited extension of Titan's energetic neutral atom (ENA) production shell. The illustration is in the  $Y = 0$  plane. Plot (a) shows the  $\vartheta = 0^\circ$  case and plot (b) shows the  $\vartheta = 30^\circ$  case. The innermost solid circle is the minimum passing distance and the outermost solid circle is the detector. The middle dashed circle is the altitude threshold above which the atmospheric density is too low for significant ENA production. Red arrowed circles are ions with pitch angles of  $90^\circ$ ; their  $\vec{E} \times \vec{B}$  drift motion has been left out of the illustration for simplicity. Green arrowed lines are representative ENA trajectories and the blue arrow is the magnetospheric background field  $\vec{B}_0$ . Regions on the detector highlighted in green receive high ENA flux, while gray regions do not. The green regions of high ENA flux rotate along the detector sphere around the  $Y$  axis (perpendicular to the plane of the figure) as  $\vartheta$  is increased from  $0^\circ$  onward. In three dimensions, these green regions form the high flux band that encircles the moon.

(see Figure 5). This increase is caused by the reduced  $\vec{E} \times \vec{B}$  drift velocity in the weaker convective electric field when the magnetic field is inclined. For  $\vartheta > 0$ , the drift velocity  $\vec{v}_D$  has a non-zero ( $+Z$ ) component:

$$\vec{V}_D = u_0(\cos^2(\vartheta)\vec{e}_X + \sin(\vartheta)\cos(\vartheta)\vec{e}_Z), \quad (9)$$

where  $\vec{e}_X$  and  $\vec{e}_Z$  are unit vectors in the  $X$  and  $Z$  directions. The magnitude of the drift velocity therefore decreases with increasing  $\vartheta$ , as

$$|\vec{v}_D| = u_0\cos(\vartheta). \quad (10)$$

Compared to its value for  $\vartheta = 0^\circ$  (120 km/s), the  $\vec{E} \times \vec{B}$  drift velocity is reduced by 13% for  $\vartheta = 30^\circ$  and by 50% for  $\vartheta = 60^\circ$ . Since the parent ions do not drift as far within one gyroperiod, the distance between successive arcs of their gyrocircles is reduced. As a result the ions may gyrate into the atmosphere more times before being thermalized or moving past Titan, increasing their path lengths through the neutral gas and their ability to emit ENAs. This effect is strongest for parent ions with pitch angles near  $90^\circ$ , as these particles' motion in uniform fields is dominated by the  $\vec{E} \times \vec{B}$  drift.

In uniform fields and for  $\vartheta = 0^\circ$  there is a sharply defined band of high ENA flux from  $-28^\circ$  to  $28^\circ$  latitude around the equator of the detector (Figure 5a). When the ambient magnetic field is inclined against the ( $-Z$ ) axis, this band retains its shape and width but is rotated around the  $Y$  axis by the same inclination angle  $\vartheta$ . In the flattened projections of the detector sphere shown in Figure 5, this rotation manifests as the increasing curvature of the band seen in Figures 5b and 5c. The ENA flux in the band (colored yellow and green) is  $\approx 1.5$ – $5$  times higher than the ENA flux into the detector above and below it (primarily colored blue) for all three values of  $\vartheta$ .

The mechanism that leads to the formation of the band of high ENA flux is illustrated in Figure 6. In our model,  $>97\%$  of the ENA flux on the detector is produced between the MPD at 1,045 km and approximately 1,800 km altitude with a peak in emissions around 1,400 km. There is thus a spherical shell in our model between

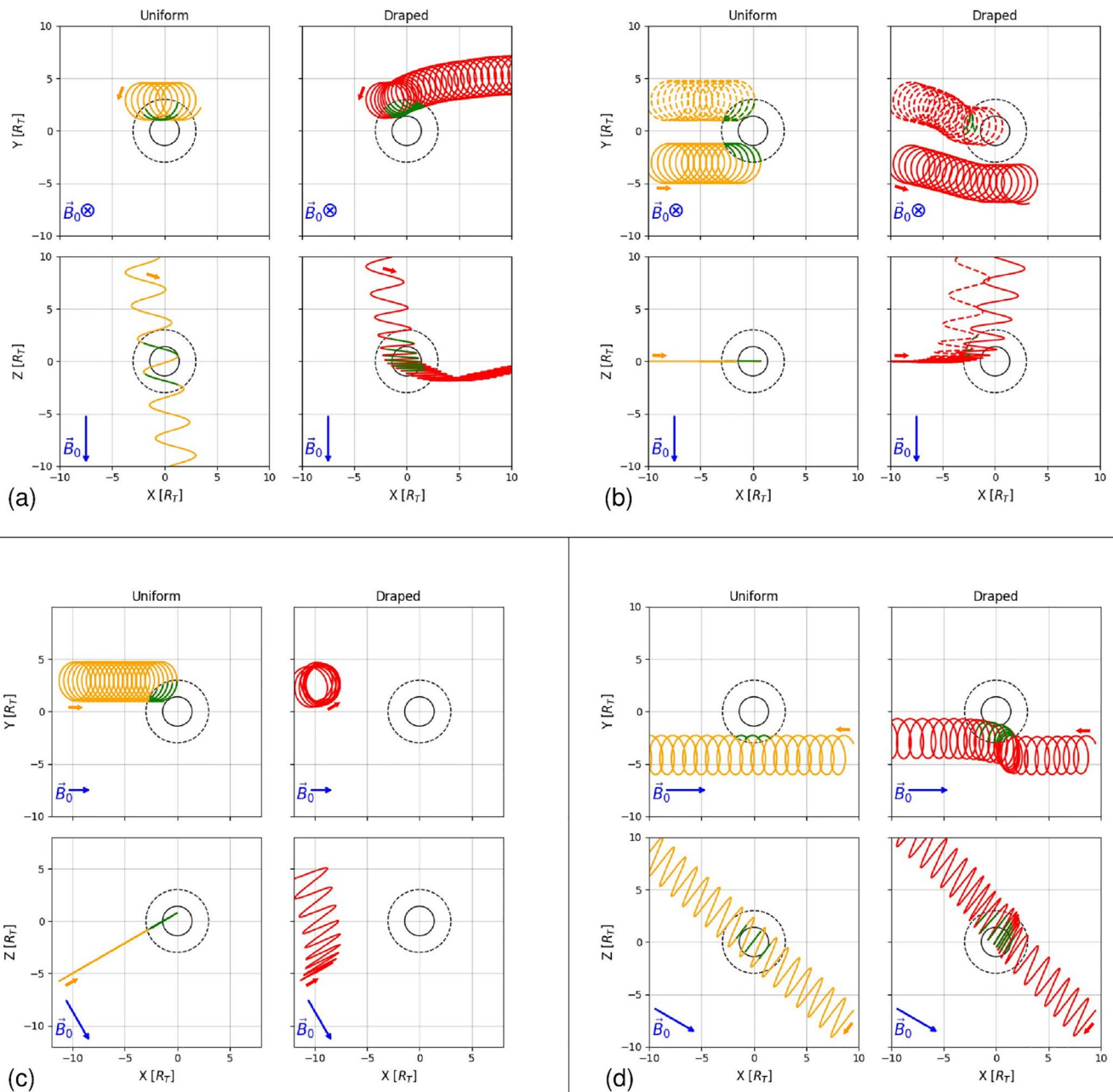


**Figure 7.** Energetic parent ion (proton) trajectories that emit energetic neutral atoms (ENAs) into various regions of interest. The lines are colored orange in uniform fields and red in perturbed fields. They are colored green when the ion is within Titan's atmosphere below the detector and above the minimum passing distance, that is, when it produces ENAs. Plots (a and b) show parent ions in the case of uninclined ( $\theta = 0^\circ$ ) background fields, and plots (c and d) show ions in the case of  $\theta = 30^\circ$  and  $\theta = 60^\circ$  inclined background fields, respectively. The columns of each of the four blocks denote uniform (left) or perturbed (right) fields. The rows within each of the four blocks are the ions' 3-D trajectories projected onto the  $Z = 0$  and  $Y = 0$  planes. The projection of the ambient magnetic field vector  $\vec{B}_0$  onto each plane is shown in blue in the bottom left of each panel. The direction of each particle along its trajectory is indicated by the small color-coded arrow near the start of each path. All ions have initial energy  $E = 30$  keV. The initial conditions of these particles are: (a)  $\vec{X} = (-0.5, 2.9, 10.0) R_T$  with velocity  $\vec{V} = (-1,629, 1,358, -525)$  km/s and pitch angle  $76^\circ$ , (b)  $\vec{X} = (-10.0, -4.0, 0.0) R_T$  with velocity  $\vec{V} = (1,199, -2,076, 0)$  km/s and pitch angle  $90^\circ$ , (c)  $\vec{X} = (-10.0, 1.0, -5.0) R_T$  with velocity  $\vec{V} = (2,076, 0, 1,199)$  km/s and pitch angle  $90^\circ$ , (d)  $\vec{X} = (9.5, -3.0, -6.6) R_T$  with velocity  $\vec{V} = (-919, 1,835, -1,033)$  km/s and pitch angle  $97^\circ$ . In panel (b), the particle with a dashed trajectory is initiated at  $\vec{X} = (-10.0, 2.0, 0.0) R_T$  with velocity  $\vec{V} = (1,199, -2,076, 0)$  km/s and pitch angle  $90^\circ$ .

1,045 km and 1,800 km where most ENAs are generated. This is a result of both the progressively higher neutral density and lower numerical weight of the parent ions as they penetrate to lower altitudes. A direct comparison between the global maps in Figure 5 and images obtained by INCA is not feasible due to the vastly different detector geometries. However, the peak emission altitude in our model is in close agreement with the peak altitude

observed during T18 (Smith et al., 2009). Garnier et al. (2010) found a mean peak emission altitude of around 2,000 km across nine earlier flybys, with observed values ranging from 5,000 km down to below 500 km. Our modeled peak emission altitude is below this mean but within the spread of measured values. The peak emission altitude in our model lies near Titan's exobase around 1,450 km altitude (Regoli et al., 2016), suggesting that most parent ions on a “downward” trajectory are neutralized into ENAs before they can penetrate into the collisional atmosphere. Since ENA production already nearly ceases within several hundred kilometers above the MPD, the sharp cutoff of emissions at this inner boundary in our model does not influence our results, that is, it does not eliminate any ENAs that would be observable in reality.

The solid gray circle in Figure 6 represents the inner radial boundary of the ENA production shell at the MPD and the dashed gray circle represents its outer boundary. The red circles in Figure 6 represent parent ions with pitch angle  $90^\circ$  which are carried by their  $\vec{E} \times \vec{B}$  drift motion into the outermost “edges” of this ENA production shell (measured along the direction of the background magnetic field). As shown in Figure 6a for  $\vartheta = 0^\circ$ , ENAs that reach the highest detector latitudes (green arrows) are produced by parent ions which travel near the apices of the sphere defined by the outer boundary of the ENA production shell, where the ambient magnetic field is perpendicular to its surface. Considering only parent ions with pitch angles near  $90^\circ$ , higher detector latitudes could only be populated by ENAs originating at higher altitudes (i.e., outside of the ENA production shell). However, the low neutral density in this region prevents significant ENA production. The result is two “polar caps” of very low ENA flux on the detector, centered around the points where the ambient magnetic field is perpendicular to the sphere, separated by a sharply pronounced band of enhanced ENA flux.

The expected latitudinal half-width  $\theta_{\text{band}, \frac{1}{2}}$  of the high flux band can be calculated from the maximum altitude of significant ENA emission  $h_{\text{max}} = 1,800$  km (see also Smith et al., 2009) and the detector radius  $R_{\text{det}} = 3 R_T$ :

$$\theta_{\text{band}, \frac{1}{2}} = \arcsin \left( \frac{h_{\text{max}} + 1 R_T}{R_{\text{det}}} \right). \quad (11)$$

This yields a band half-width of  $35^\circ$ , near the  $28^\circ$  half-width seen in the first row of Figure 5. The modeled flux band is narrower than the geometric estimation predicts because the parent ion gyroplanes only briefly intersect the ENA production shell near its apices. This limits ENA emissions into the upper and lower edges of the predicted flux band. The agreement between the model in Figure 6 and the particle tracing model suggests that, for uniform fields, the high flux band is primarily produced by parent ions with pitch angles near  $90^\circ$ .

In all three ENA maps in the first row of Figure 5, the high flux band contains  $\approx 1.5$  times more ENA flux in the (+Y) hemisphere (from  $270^\circ$  to  $90^\circ$  longitude) than in the (−Y) hemisphere (from  $90^\circ$  to  $270^\circ$  longitude). As illustrated by the two sample ion trajectories in the left panel of Figure 7b, parent ions with pitch angles near  $90^\circ$  are thermalized before reaching the downstream portion of Titan's atmosphere. This is evident in both the  $Y > 0$  and  $Y < 0$  half spaces. The effect of this thermalization on the ENA morphology is asymmetric due to the sense of the ions' gyration around the magnetic field. It can be seen from the green portions of the trajectories in the left column of Figure 7b that ENAs are emitted in the *same* direction in both Y half spaces. As nearly all of the green arcs have tangents pointing toward (+Y), both ions shown emit ENAs almost exclusively into the (+Y) hemisphere. If they continued farther into the  $X > 0$  half space, these ions would travel through the atmosphere in a different portion of their gyromotion and would emit ENAs along tangents pointing toward (−Y) as well. However, the ions are thermalized before this occurs. The result of many such particles is the ( $\pm Y$ ) flux asymmetry seen in the first row of Figure 5. In a hypothetical case where the direction of the ambient magnetic field was reversed, the ENA flux would be more intense in the (−Y) hemisphere.

While parent ions with pitch angles near  $90^\circ$  are unable to populate the “polar caps” with ENAs, these regions display non-negligible flux in Figures 5a–5c. These contributions to the ENA emissions are generated by parent ions with pitch angles away from  $90^\circ$ . Such particles have field-aligned velocity components which may become comparable to their gyration and drift velocities. A sample ion with a pitch angle of  $76^\circ$  is shown in Figure 7a in uniform fields with  $\vartheta = 0^\circ$  (left column, orange line). As shown by the green arcs of its trajectory, this particle emits ENAs into the  $Z < 0$  “polar cap” region between  $0^\circ$  and  $90^\circ$  longitude (dark blue in Figure 5a).

The flux disparity between the “polar caps” and the equatorial band is a result of a discrepancy in the “ability” of ions to emit ENAs based on their pitch angles. The  $\vec{E} \times \vec{B}$  drift velocity ( $V_D \leq 120$  km/s) is low compared to the ions' initial velocities ( $V = \sqrt{2E/m_p} \approx 2400$  km/s). With their drift motion displacing their guiding centers

by  $\approx 0.1 R_T$  over one gyroperiod and with gyroradii of  $\approx 2 R_T$ , parent ions with pitch angles near  $90^\circ$  may traverse the ENA production shell and emit ENAs over many gyrations. For example, the solid ion trajectory shown in the left column of Figure 7b has a pitch angle of  $90^\circ$  and emits ENAs during a portion of five consecutive gyroperiods before being thermalized below the MPD. The displacement is reduced even further when  $\vartheta > 0^\circ$  due to the slower  $\vec{E} \times \vec{B}$  drift. For  $\vartheta = 60^\circ$  the  $\vec{E} \times \vec{B}$  drift velocity is only 50% of its value for  $\vartheta = 0^\circ$  (see Equation 10). The resulting large amount of ENA flux emitted by ions with pitch angles near  $90^\circ$  mostly populates the high flux band of the detector sphere. By contrast, parent ions with large magnetic field-aligned velocities, such as the ion shown in the left column of Figure 7a, traverse the ENA production shell during a portion of only one or two gyrations. Ions such as these, which populate the “polar caps” of the detector sphere, emit fewer ENAs than those with pitch angles near  $90^\circ$ .

The global ENA flux maps for perturbed fields are shown in the second row of Figure 5. The field perturbations that form the induced magnetosphere have a clear influence on the intensity of Titan's ENA emissions. When field line draping is included, the ENA flux integrated over the entire detector sphere is reduced by approximately 31%, 38%, and 36% compared to uniform fields in the  $\vartheta = 0^\circ$ ,  $30^\circ$ , and  $60^\circ$  case, respectively. The reduced ENA emissions in perturbed fields are due in part to the magnetic field enhancement upstream of Titan (Figures 4d–4f) shielding the moon from a significant portion of energetic parent ions with pitch angles near  $90^\circ$ .

In uninclined ( $\vartheta = 0^\circ$ ) fields, the most notable difference between the uniform and perturbed cases (Figures 5a and 5d, respectively) is the  $\approx 45\%$  reduction in flux detected within the equatorial band when field draping is included. This reduction appears as the blue equatorial band in Figure 5g. The ion trajectories in Figure 7b, launched with initial pitch angles of  $90^\circ$ , illustrate the shielding effect of the pileup region that largely causes this reduction. In uniform fields (left panel) these particles drift solely toward (+X), enter the ENA production shell, and emit ENAs. In draped fields, however, the ions are redirected away from Titan toward (–Y) and (+Z) and do not enter the ENA production shell. As they approach the moon and enter the ramside pileup region at  $X \approx -4 R_T$ , these ions gain a gradient drift velocity  $\vec{V}_V$  given by

$$\vec{V}_V = \frac{mV_\perp^2}{2qB^3} (\vec{B} \times \nabla B), \quad (12)$$

where  $V_\perp$  is the ion's velocity perpendicular to the magnetic field and  $\nabla B$  is the gradient of the field magnitude. In the  $\vartheta = 0^\circ$  case, the magnetic field gradient at the upstream side of the pileup region primarily points in the (+X) direction (see Figure 4d), while the field in the pileup region points in the (–Z) direction. Thus, the gradient drift velocity points toward (–Y), causing the ions in Figure 7b to be diverted toward the (–Y) side. Ions initially located in the  $Y > 0$  half space are therefore deflected toward Titan, while ions that originate at  $Y < 0$  are deflected away from the moon.

These ions also gain velocity antiparallel to the background magnetic field (i.e., in (+Z) direction) as they pass through the pileup region. Similar trajectories to this were produced by Wulms et al. (2010) and Kabanovic et al. (2018); the shielding of such ion trajectories is even visible in ENA images produced by Kabanovic et al. (2018) for the TA flyby, where it produces an equatorial gap in the ENA emissions that reach their plane detector (Figure 11d therein). The significant attenuation of the high flux band in Figure 5d is mainly a result of the deflection of these parent ions by the ramside field gradient.

As shown by both Cassini data and our model, the ramside field strength decreases immediately downstream of the strongest magnetic enhancement. Therefore, the field gradient instead points in the (–X) direction just above the MPD (see Figure 4d). The particle in the right panels of Figure 7a has a velocity component parallel to the ambient magnetic field that is over 5 times larger than its  $\vec{E} \times \vec{B}$  drift velocity, so it descends toward Titan from (+Z) rather than approaching from directly upstream. Its guiding center reaches the moon downstream of the ramside pileup, but still above the MPD, where the “reversed” field gradient deflects it toward (+Y).

Figures 5e and 5f show the global flux maps for draped fields in the  $\vartheta = 30^\circ$  and  $60^\circ$  case, respectively. The qualitative features in the ENA emissions remain largely unchanged from the uniform fields cases in Figures 5b and 5c. As the field inclination increases, however, the field line draping has a progressively weaker impact on the intensity of the ENA flux emitted into the high flux band. This is evident from comparing the larger ENA flux differences colored dark blue and red in the equatorial band in Figure 5g to the smaller differences colored light blue and white in the band in Figure 5i. In other words, ENA emissions are more intense when Titan is away from

the center of the magnetodisk than when it resides within the magnetodisk current sheet. The intensity of the high flux band is reduced by about 40% compared to the uniform field case for  $\vartheta = 30^\circ$  and by about 23% compared to uniform fields for  $\vartheta = 60^\circ$ .

The smaller attenuation effect of the field perturbations on the high flux band for  $\vartheta > 0^\circ$  is a consequence of the rotated and stretched shape of the pileup region, the weaker magnetic enhancement in the pileup, and the asymmetry of Titan's magnetic lobes between the ( $\pm Z$ ) half spaces. The field inclination rotates the  $\vec{E} \times \vec{B}$  drift velocity and the parent ions' gyroplanes. Figure 7c shows the trajectory of a particle with an initial pitch angle of  $90^\circ$  for  $\vartheta = 30^\circ$ . In uniform fields (left panels), the ion drifts toward downstream and ( $+Z$ ) with a velocity of  $\vec{E} \times \vec{B}/B^2 = \{90, 0, 30\sqrt{3}\}$  km/s. It enters the atmosphere during about 6 gyroperiods and emits ENA flux before being thermalized below the MPD. This ion contributes to the high flux band in Figure 5b. In draped fields (right panels of Figure 7c), an ion launched with the same initial conditions is deflected antiparallel to the magnetic field upstream of Titan. This deflection occurs at the outer edge of the region where the field lines begin to pile up (colored dark green near  $X = -5 R_T$  in Figure 4e). The selected ion leaves the simulation domain well before reaching the moon and does not emit any ENAs at all in perturbed fields. Kabanovic et al. (2018) found similar ion trajectories which were strongly affected by even the rather weak field perturbations between 5 and  $10 R_T$  upstream or to ( $\pm Y$ ) of Titan, due to the stretching of the pileup region along the outer flank of the pick-up tail (Figure 6 therein).

The radial "thickness" of the pileup region and the strength of the field gradient determine the ions' ability to access the ENA production shell. For  $\vartheta = 30^\circ$ , the maximum field enhancement in the pileup region is reduced by 15% compared to the  $\vartheta = 0^\circ$  case. This reduction, which lowers the gradient drift velocity proportionally (Equation 12), only minimally weakens the parent ion deflection. Thus, the ramside field enhancement is still able to strongly attenuate the high flux band (Figure 5e). However, the peak field is enhanced by only about half as much when  $\vartheta = 60^\circ$  (peak value of  $1.35 B_0$ ) as when  $\vartheta = 0^\circ$  (peak value of  $1.62 B_0$ ). The gradient drift velocity of parent ions in this case is correspondingly halved, significantly lessening the deflection of these particles away from Titan. The weaker pileup fields are therefore less able to shield the atmosphere from the parent ions that contribute the most ENAs to the high flux band, giving the  $\vartheta = 60^\circ$  flux map (Figure 5f) the strongest ENA signature within the high flux band of the perturbed fields cases.

Despite the weakened shielding in inclined fields, the field draping still globally reduces the ENA flux produced in every case. This appears somewhat counter to the results of Wulms et al. (2010) and Kabanovic et al. (2018). Approximating the TA flyby viewing geometry, both of these studies found instances of locally *increased* ENA flux, as well as shifts in regions of maximum and minimum flux, when the field draping is included (see, e.g., Figure 15 in Wulms et al., 2010). However, such enhancements were not present in all viewing directions of the plane detector, which selects for a narrow range of ENA velocity vectors nearly parallel to its normal. While a detector with a specified viewing direction or limited field of view may measure locally increased ENA flux, the field line draping in general does not enhance global ENA emissions above the levels in uniform fields.

While the field enhancement reduces the emissions of parent ions with pitch angles near  $90^\circ$ , it simultaneously *increases* the emissions of certain parent ions that approach along the magnetic field. The highest ENA flux detected in each of the draped field cases encompasses several faint filamentary features embedded within the high flux band. Despite the globally reduced flux in perturbed fields, the flux in these local regions is equal to or even slightly greater than in the uniform fields cases. The filamentary enhancements are most visible in the difference plots in the third row of Figure 5, where they are colored white or red. For  $\vartheta = 0^\circ$ , these features appear light blue and green in the equatorial region of Figure 5d. Parent ions such as the one shown in the right panels of Figure 7a contribute to these regions of locally elevated ENA flux. That ion descends into the field enhancement above Titan's ( $+Z$ ) hemisphere (colored red in Figure 4d). The increasing field strength produces a magnetic mirror force that reduces the ion's  $|V_z|$  velocity magnitude by a factor of 150 while it is located within  $2 R_T$  of the MPD. This deceleration decreases the distance between consecutive spiral arcs of its trajectory (visible in the lower right panel of Figure 7a). This parent ion then gyrates at low latitudes within the atmosphere about 7 times (where the trajectory is colored green), emitting ENAs primarily into low latitudes of the ( $+Y$ ) hemisphere of the detector (from  $270^\circ$  to  $90^\circ$  longitude) and contributing to the filamentary features in Figure 5d. A portion of the ENAs emitted by this select ion are detected in the region within one of these filaments outlined in red at  $7^\circ$  latitude and  $34^\circ$  longitude. The parent ion then exits the interaction region within the magnetic neutral region

(white in Figure 4a) after bouncing off of the enhanced magnetic field in the ( $-Z$ ) lobe of the induced magnetosphere around  $5 R_T$  downstream.

Similar filamentary enhancements are present within the high flux band formed in perturbed fields for  $\vartheta > 0^\circ$ , colored light blue/green in Figures 5e and 5f and white in Figures 5h and 5i. These structures are again created by ions that mainly move along the magnetic field. The pileup region is rotated toward ( $-Z$ ) for both  $\vartheta = 30^\circ$  and  $60^\circ$ . However, the shape of the field enhancement within  $2 R_T$  of the moon is still very similar between the  $\vartheta = 0^\circ$  and  $\vartheta = 30^\circ$  cases (see Figures 4d and 4e). While the ( $+Z$ ) pole of Titan is somewhat less protected by the pileup in the latter case, ions with guiding centers that descend along the magnetic field in the  $Z > 0$  half space are still carried into the ramside field enhancement by their large gyroradii ( $\approx 2 R_T$ ). Parent ions with significant field-aligned velocities are therefore decelerated by the field enhancement and emit ENAs into the filamentary structures in Figure 5e in much the same manner as in uninclined fields. For  $\vartheta = 60^\circ$ , however, the pileup region is rotated nearly entirely into the  $Z < 0$  half space and is dragged about  $5 R_T$  downstream (see Figure 4f). In the same way, the magnetic neutral region (light blue in Figure 4f) is rotated into high latitudes in the  $Z > 0$  half space and is no longer located within Titan's geometric plasma shadow. Parent ions which originate upstream in the  $Z > 0$  half space and possess a velocity component parallel to the magnetic field pass through this region of reduced field strength. Their gyroradii are increased, causing them to more easily gyrate around Titan and miss the ENA production shell as they pass by.

Conversely, in the  $\vartheta = 60^\circ$  case ions which originate *downstream* of Titan and approach with a velocity component antiparallel to the magnetic field are strongly decelerated by the field enhancement in the ( $-Z$ ) hemisphere. These particles may have their path length within the atmosphere extended by the field draping (analogous to the ion trajectory shown in Figure 7a), if they can penetrate through the pileup region, and emit ENAs that contribute to the filamentary features in Figure 5f. Figure 7d displays the trajectory of such an ion with an initial pitch angle of  $97^\circ$ . While this particle's drift motion is directed toward downstream ( $\vec{E} \times \vec{B} / B^2 = \{30, 0, 30\sqrt{3}\}$  km/s), the magnitude of the drift velocity is only 50% of its value in the uninclined case (see Equation 10). The component of the ion's translation velocity antiparallel to the magnetic field ( $\approx 290$  km/s) is a factor 5 larger than the  $\vec{E} \times \vec{B}$  drift velocity perpendicular to it, so the particle is easily able to travel toward upstream and reach Titan.

In uniform fields (left panels of Figure 7d) this ion only gyrates through the rarefied upper atmosphere three times and emits less than 1% of its numerical weight as ENA flux. However, in perturbed fields (right panels) it gyrates through the atmosphere eight times, passes through the ENA production shell (i.e., the much more dense neutral gas close to the MPD), and emits  $\approx 94\%$  of its numerical weight. Since the emissions in draped fields occur after the ion has lost around 73% of its velocity along the ambient magnetic field, the resulting ENAs travel largely perpendicular to the field. Since they are emitted from the downstream portion of the production shell's ( $-Y$ ) hemisphere, these ENAs contribute to the high flux band in the ( $-Y$ ) hemisphere of the detector (primarily at negative latitudes). Some of this flux is detected within the region outlined in red at  $-25^\circ$  latitude and  $210^\circ$  longitude in Figure 5f. As the ion travels from the enhanced fields in the pileup region (at  $Z < 0$ ) into the reduced fields in the neutral region above Titan's ( $+Z$ ) hemisphere, it regains  $\approx 57\%$  of its initial field-aligned velocity and escapes the interaction region. Ions with such decelerated helical trajectories produce the filamentary structures found in the high flux band in Figure 5f.

Both the ambient field inclination and the field draping very clearly influence Titan's global ENA emission morphology. Furthermore, the effect of the field perturbations on the ability of each parent ion to emit ENAs is highly dependent on its pitch angle. While our global ENA maps cannot be directly compared to INCA observations due to the drastically different detector geometries, the field perturbations near Titan have outsized influence them both. Garnier et al. (2010) found that variations in the observed ENA emissions across 11 Cassini flybys were driven by parent ion dynamics, which are governed by the upstream fields and Titan's plasma interaction, and not by exospheric dynamics. The strong influence of the field perturbations on the ENA signature thus manifests in both the heavily truncated ENA population imaged by INCA and in the global ENA distribution captured by our model detector. Despite this, our model suggests that the net effect of the field line draping is mainly to reduce the intensity of Titan's ENA emissions and not to drastically change the ENA morphology (see Figure 5). A reduction in the upstream bulk velocity from 120 km/s to 80 km/s (as suggested by Thomsen et al. [2010] and Kane et al. [2020]) would only weaken the strength of the draping (see Figure 17c in Simon et al. [2006]). The

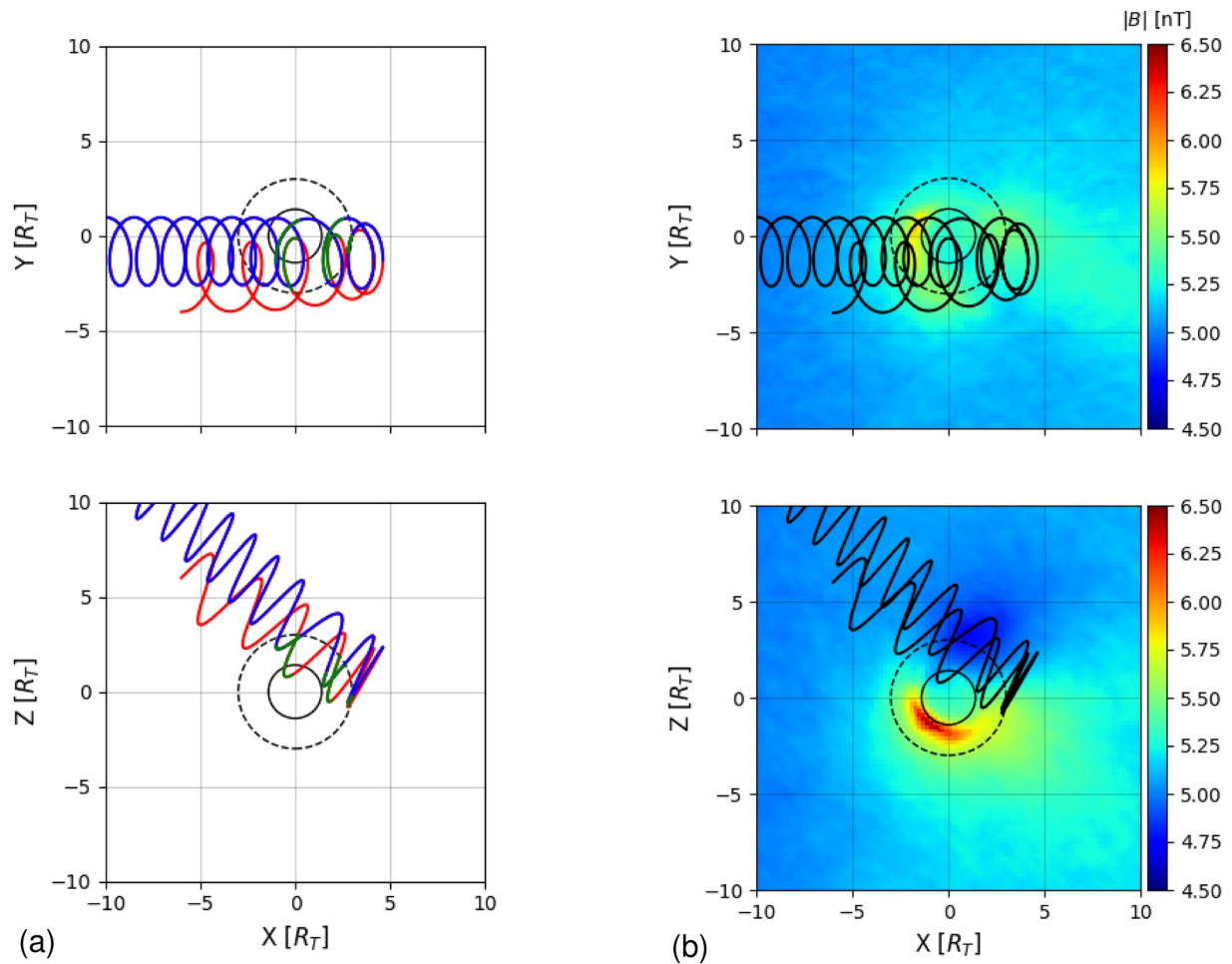


**Figure 8.** Trajectory of an energetic parent ion that is reflected by the magnetic field enhancement in the downstream portion of the pileup region in the  $\theta = 60^\circ$  case. The ion is initialized at  $\vec{X} = (-6, -4, 6) R_T$  with velocity  $\vec{V} = (1,695, 0, 1,695)$  km/s, corresponding to an energy of 30 keV and a pitch angle of  $75^\circ$ . In plot (a) the path is red when the guiding center motion is toward downstream, blue when it is toward upstream, and green when the particle passes within the moon's atmosphere above the minimum passing distance (producing energetic neutral atoms). Plot (b) shows the same ion's trajectory overlaid on the magnetic field magnitude from AIKEF. The field values shown are from the  $Z = 0$  and  $Y = 0$  planes onto which the particle trajectory is projected.

expected effect on the ENA maps would therefore be a quantitative increase in ENA emission intensity in the draped fields, rather than a qualitative effect on the ENA morphology.

The trajectories of select parent ions are altered by the perturbed fields even more drastically than those shown in Figure 7. For instance, we identified parent ions that travel toward downstream and initially pass Titan, but are then reflected back toward upstream by magnetic mirror forces. One such particle trajectory is shown in Figure 8 for draped, inclined ( $\theta = 60^\circ$ ) fields. This ion passes through the reduced magnetic field in the neutral region above Titan's (+Z) hemisphere (dark blue in the lower panel of Figure 8b). Its guiding center motion is slowed and ultimately reversed as it encounters the magnetic enhancement in the portion of the pileup region that has been rotated and stretched into Titan's geometric plasma shadow (light green and yellow). This reflection occurs after the ion has already passed through the ENA production shell during two gyroperiods and emitted ENAs. After being reflected by the pileup region at the moon's *downstream* side, the ion in Figure 8 reenters the production shell on its way back toward upstream and makes a second "pass" at generating ENAs. We remind the reader that each ion macroparticle in our model represents a large number of real energetic parent ions. Thus, the ENAs emitted during this second "pass" are products of the neutralization of real ions (represented in bulk by this macroparticle) which previously escaped the ENA production shell, either without undergoing charge exchange or after being neutralized and then re-ionized.

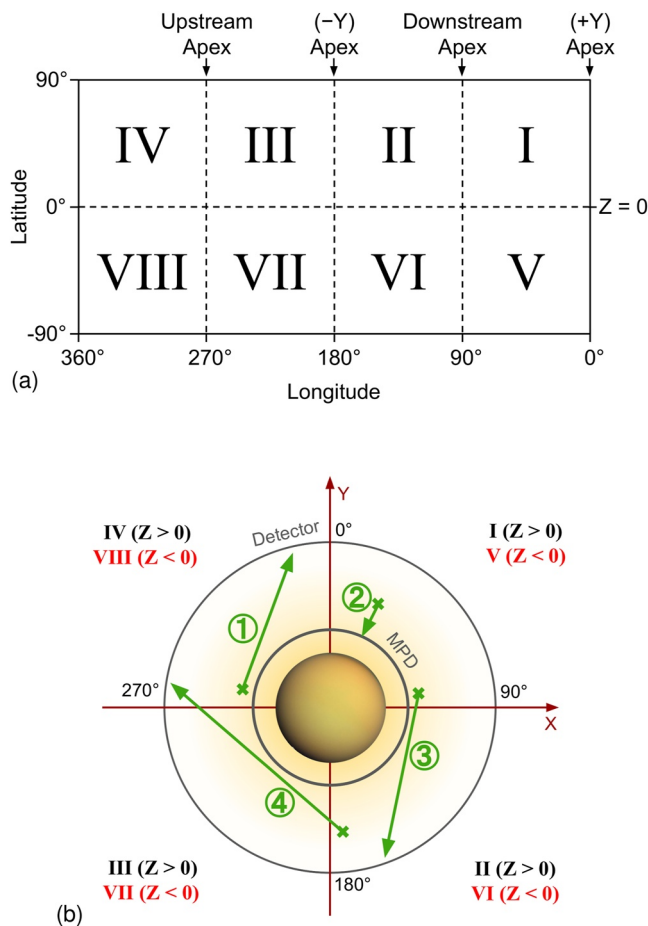


**Figure 9.** Modeling the correlation between energetic neutral atom (ENA) emission and ENA detection: (a) Octants of the region where ENAs are produced in the rotated West Longitude coordinate system. Labeling of the three-dimensional production octants (I-VIII) starts at  $0^\circ$  longitude and proceeds westward (i.e., with increasing longitude) around the moon, first in the  $Z > 0$  hemisphere (positive latitudes), then in the  $Z < 0$  hemisphere (negative latitudes). The  $(\pm Y)$ , upstream, and downstream apices of the spherical shell are labeled for reference. (b) Several hypothetical ENA trajectories projected onto the  $Z = 0$  plane of the DRAP coordinate system. Longitude on the detector sphere is given at each axis. The location where each ENA is produced is denoted by a green  $\times$ . The ENAs travel in a straight line until they either reach the detector or are thermalized below the minimum passing distance (MPD). The production octants are labeled in black above  $Z = 0$  and in red below  $Z = 0$ . ENA ① is detected locally above its production octant, ENA ② passes below the MPD and is thermalized, and ENAs ③ and ④ are detected non-locally in detector hemispheres away from their production octants.

Parent ions with helical trajectories, like the one in Figure 8, could in principle follow the magnetospheric field lines all the way to Saturn's polar region and bounce back toward Titan for a third "pass." Regoli et al. (2016) estimated that a gyrating 30 keV  $H^+$  ion which translates along the magnetospheric field, bounces, and returns to Titan's local interaction region has an azimuthal displacement of approximately  $\Delta X = 6 R_T$ . Such an ion may return close enough to make a third "attempt" at producing ENAs. In our model, we initialize parent ion macroparticles according to the observed velocity distribution at the  $(\pm Z)$  and  $(\pm X)$  faces of the simulation domain. This distribution inherently contains ions that are returning to Titan's interaction region after bouncing. Therefore it is not necessary to model the full bounce motion of these ions in the particle tracing code.

Although they may produce ENAs during several distinct "passes" at Titan, parent ion macroparticles like the one shown in Figure 8 in general only contribute significantly to the global ENA emission pattern during the first "pass" that intersects the ENA production shell. The ENA flux a parent ion emits as it moves through the atmosphere is a function of its instantaneous numerical weight (Equation 7), that is, the number of real ions that the macroparticle represents. Consequently, a reflected parent ion will generally emit greater flux during its first "pass" through the ENA production region than during any subsequent "passes" due to it being already partially attenuated. For instance, the parent ion macroparticle shown in Figure 8 emits about six times more ENA flux while it is moving toward downstream than after it is reflected back toward upstream.

### 3.3. Correlation Between ENA Production and Detection Regions

The global ENA maps discussed in Section 3.2 only indicate the locations where ENAs ultimately reach the detector sphere (i.e., where they leave after traveling away from their point of production). They do not contain information on the origin of the detected ENAs. To constrain the regions of ENA production that create the modeled ENA features in Figure 5, we subdivide the production region (inner radius  $R_{MPD} = 1.4 R_T$ , outer radius  $R_{det} = 3 R_T$ ) into eight sectors (hereafter called "production octants"). These octants are defined in Figure 9a. Subsequently we decompose the global ENA maps from Figure 5. Each decomposed map displays the flux through the entire surface of the detector sphere. However, in each of these eight maps only the contribution of ENA flux that is generated within one specific octant of the production shell is shown. The full ENA map (as displayed in Figure 5) can be reconstructed by taking the sum of the eight maps corresponding to the eight production octants. In this way, we can recover information on the origins of individual structures in the global ENA emission morphology, such as the band of high ENA intensity along the equator in Figure 5a.

Since ENAs may travel several  $R_T$  before reaching the spherical detector, they are not necessarily detected close to where they are produced. To illustrate

this process, Figure 9b depicts the production and detection of several hypothetical ENA trajectories. ENA ① is detected above the production octant where it was created, that is, it is detected locally. ENA ② moves toward Titan, is thermalized below the MPD, and does not contribute flux on the detector sphere. ENA ③ is detected non-locally from its production octant, though within the same hemisphere (downstream,  $X > 0$ ) that it was produced. ENA ④ is also detected non-locally, far from the production octant where it originated.

The production octants (Figure 9a) are labeled with Roman numerals I through VIII according to the rotated West Longitude coordinate system described in Section 2.4. The labels proceed from  $0^\circ$  up to  $360^\circ$  longitude, at positive latitudes ( $Z > 0$ , labeled I-VI) then negative latitudes ( $Z < 0$ , labeled V-VIII). A map of the ENA

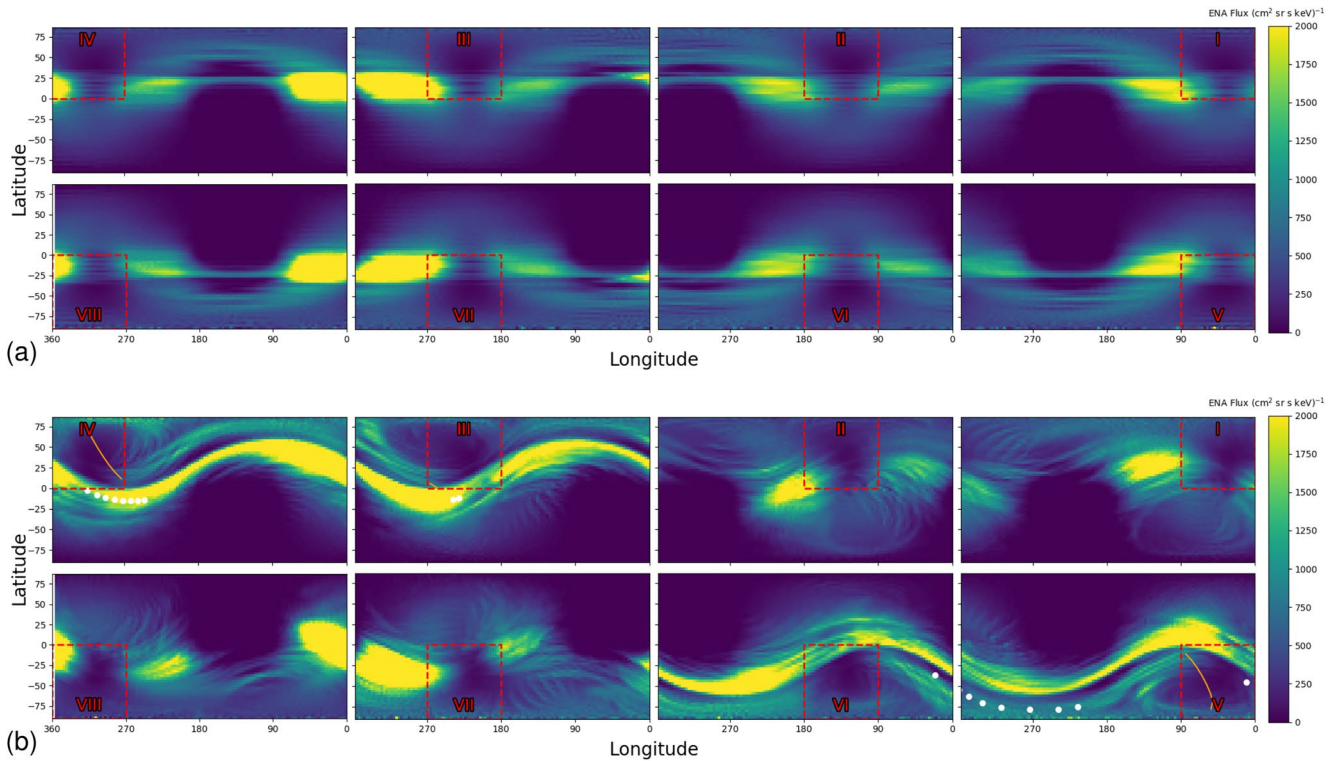


**Figure 10.** (a) Energetic neutral atom (ENA) flux maps for ENA production within eight regions of the atmosphere in the  $\vartheta = 0^\circ$  case for uniform fields. The octants are defined by the rotated West Longitude coordinate system. The portion of the detector which lies directly above the production octant shown in each panel is outlined by a red dashed box. ENAs that reach this outlined region of the detector (a curved sector of the actual sphere) are detected locally, above the octant of the spherical shell in which they are produced. The decomposed ENA maps are arranged according to the latitudes and longitudes occupied by their associated production octants, shown in Figure 9a. For instance, the detector map of ENAs produced in octant I is located at the top right of the Figure, the map of ENAs produced in octant II is to its left, and so on. (b) ENA flux maps for production within eight regions of the atmosphere in the  $\vartheta = 30^\circ$  case for uniform fields. The octants are defined and labeled in the same manner as in panel (a). The orange lines trace out the path of the parent ion shown in Figure 11a through each production octant, projected radially onto the surface of the detector sphere. The lines are only shown where the parent ion passes within the ENA production shell above the minimum passing distance, that is, they correspond to the green trajectory segments in Figure 11a. The white dots indicate where ENAs emitted by the ion in each octant were detected.

flux through the *full* detector sphere is produced for each octant of the atmosphere, that is, for one-eighth of the production region. For instance, Figure 10a shows the decomposed ENA maps for uniform fields in the  $\vartheta = 0^\circ$  case. The upper right-most panel shows the flux (through the *entire* detector) of ENAs produced between  $0^\circ$  and  $90^\circ$  longitude and  $0^\circ$ – $90^\circ$  latitude, at all altitudes between the MPD and the detector (octant I in Figure 9a). Due to their travel after being produced in this octant, many of these ENAs are detected non-locally across a wide range of latitudes and longitudes on the detector sphere. The production octant of the ENA flux shown in this panel of Figure 10a, octant I, is outlined by the dashed red line and labeled in the same manner as in Figure 9a. In each panel, ENA flux within the region outlined in red reaches the detector above the same production octant where it originated.

We discuss only the  $\vartheta = 0^\circ$  and  $\vartheta = 30^\circ$  cases here, as these two are sufficient for discerning the physics governing the origins of ENA emissions for both uninclined and inclined upstream magnetic fields. The production octants in the  $\vartheta = 60^\circ$  uniform fields case qualitatively show the same features as in the  $\vartheta = 30^\circ$  uniform fields case (Figure 10b) with contributions to, for example, the high flux band reaching higher latitudes due to the band's rotation around the *Y* axis (compare Figure 5b and Figure 5c). The production octants in the  $\vartheta = 60^\circ$  draped fields case maintain the same major features as in the uniform fields case, with a quantitative decrease in ENA production in all octants (see Figures 5c and 5f).

The panels of Figure 10a illustrate how each production octant contributes a portion of the equatorial high ENA flux band seen in Figure 5a. The highest ENA flux from each octant reaches the detector in a region approximately  $90^\circ$  of longitude wide and  $28^\circ$  of latitude tall (the same height as the half-width of the high flux band in Figures 5a–5c). For instance, this region is bright yellow from  $90^\circ$  to  $180^\circ$  longitude and  $0^\circ$ – $28^\circ$  latitude for

production octant I in Figure 10a. Each of these flux contributions is located within the same  $Z$  half space as the production octant where it originates (denoted by the red dashed lines). This confirms that the ENAs detected within the high flux band are emitted by parent ions with pitch angles near  $90^\circ$ , giving them only a small  $V_z$  velocity component and effectively “slicing” the contributions to the high flux band in half at the equator ( $Z = 0$ ). Due to the ions' counter-clockwise sense of gyration, their most intense ENA emissions are therefore observed approximately  $90^\circ$  displaced toward higher longitudes (i.e., westward) from where they are generated, with little displacement in latitude.

In Figure 10a the most intense contributions to the high flux band are produced in octants III, IV, VII, and VIII, that is, in the upstream ( $X < 0$ ) hemisphere of the production region. For example, the elevated flux region detected adjacent to production octant III (outlined in red) is larger and more intense than that associated with production octant II. The strong contributions to the high flux band generated in octants III, IV, VII, and VIII travel toward higher longitudes into the ( $+Y$ ) hemisphere of the detector, while the lower flux produced in the downstream ( $+X$ ) hemisphere of the atmosphere (production octants I, II, V, and VI) travels into the ( $-Y$ ) hemisphere of the detector. The higher intensity of the equatorial flux band in the ( $+Y$ ) hemisphere compared to the ( $-Y$ ) hemisphere of the detector (see Figure 5a) is therefore a consequence of higher ENA production in the upstream ( $-X$ ) hemisphere compared to the downstream ( $+X$ ) hemisphere of the production shell (see Figure 10a). In other words, the detectable longitudinal asymmetry in ENA flux is rotated approximately  $90^\circ$  of longitude clockwise from where the associated ENAs are produced.

This emission of ENAs toward higher longitudes is visible in the individual particle trajectories displayed in Figure 7. As illustrated by the green portions of the two ion trajectories in the left panel of Figure 7b, such parent ions move toward higher longitudes at the portion of their gyromotion that reaches the lowest altitude. Assigning ENAs generated in the  $Z = 0$  plane to the ( $+Z$ ) half space, the solid parent ion trajectory produces ENAs in octant III of Figure 10a that contribute to the high ENA flux (bright yellow) near  $270^\circ$  longitude (the ( $-X$ ) apex of the detector). The dashed ion trajectory produces ENAs in octant IV of Figure 10a that contribute to the high ENA flux near  $0^\circ$  longitude (the ( $+Y$ ) apex of the detector).

There is also a similar, but more faint, region of elevated ENA flux at lower longitudes (i.e., eastward) adjacent to each production octant in Figure 10a. These ENA detections are also a part of the equatorial high flux band (see Figure 5a). However, they are produced during the opposite portion of the parent ions' gyrocircles. The solid ion trajectory in the left panel of Figure 7b produces ENAs in octant III which travel toward the upstream apex, contributing to the higher flux detected in clockwise direction (westward) from the production region. However, this specific ion cannot emit ENAs toward the east.

Figure 11 shows two additional selected parent ion trajectories, panel (a) in  $\vartheta = 0^\circ$  fields and panel (b) in  $\vartheta = 30^\circ$  fields. The parent ion trajectories shown in the left columns of Figures 7a and 11b demonstrate how ENAs that contribute to the eastward “patch” of elevated flux are generated. The ion in Figure 7a spirals toward Titan from the ( $+Z$ ) half space with a pitch angle of  $76^\circ$ . It can gyrate around the sphere defined by the MPD and avoid thermalization due to its velocity parallel to the magnetic field ( $V_{\parallel} \approx 621$  km/s compared to  $V_D = 120$  km/s) and its large gyroradius ( $R_g = 1.9R_T$  compared to  $R_{MPD} = 1.4R_T$ ). Such parent ions may produce ENAs in nearly every segment of their gyration, contributing ENA flux to the elevated flux regions on either side of the production octants in Figure 10a. For instance, the ion in Figure 7a emits ENAs to the west of octants IV and VIII.

The ion in Figure 11b travels along a similar trajectory and with the same pitch angle ( $75^\circ$ ) in  $\vartheta = 30^\circ$  fields. It completes nearly two full gyrations within the atmosphere, though only a portion of each reaches the dense neutral gas at low altitudes above the MPD. The orange lines in Figure 10a are this ion's trajectory through the ENA production shell in each octant, projected radially onto the detector sphere. For each octant, the locations where the ENAs it emits strike the detector are indicated by white dots. This ion produces its strongest emissions in octant IV, which are detected within the high flux band to the east of the red outlined production region (colored yellow) in octant IV of Figure 10a; and in octant V, which are detected in the region of “background” flux east of the production region at high negative latitudes (colored light blue).

In aggregate, ions that gyrate around the moon in uniform fields due to their large velocities parallel to the field lines emit similar numbers of ENAs to the east and to the west. Parent ions with pitch angles near  $90^\circ$ , meanwhile, only emit ENAs into the region at higher longitudes (westward) from the respective production octant. Furthermore, the latter group of ions emit more ENA flux due to their greater path lengths through the production shell.

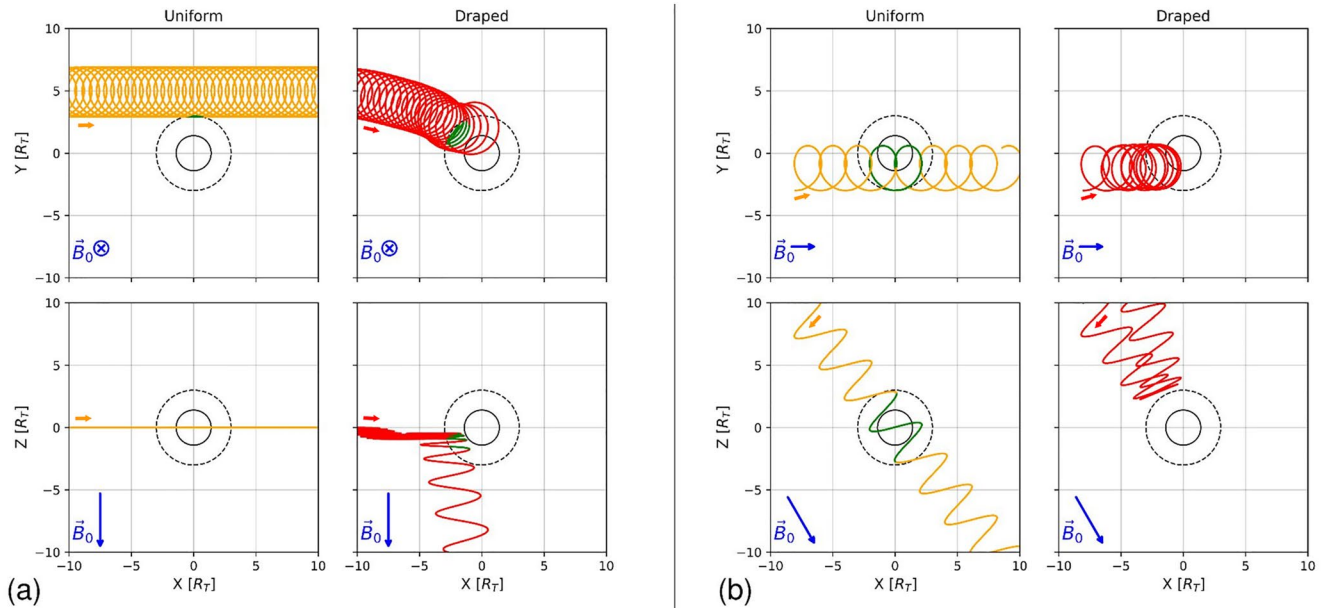


**Figure 11.** Energetic parent ion trajectories in several (uniform and draped) field geometries. The plots are formatted in the same manner as in Figure 7. Plot (a) shows a pair of ion trajectories through uninclined ( $\vartheta = 0^\circ$ ) fields and plot (b) shows a different pair of trajectories through  $\vartheta = 30^\circ$  inclined fields. The initial conditions of these particles are: (a)  $\vec{X} = (-10.0, 5.0, 0.0) R_T$  with velocity  $\vec{V} = (0, 2,397, 0)$  km/s and pitch angle  $90^\circ$ , (b)  $\vec{X} = (-8.0, -3.0, 10.0) R_T$  with velocity  $\vec{V} = (2,316, 0, 620)$  km/s and pitch angle  $75^\circ$ . All particles have initial energies of  $E = 30$  keV.

As a result, the region westward of each production octant in Figure 10a receives approximately 1.5–2 times higher ENA flux than the region to the east. These fragmentary contributions to the high flux band can therefore be associated with specific sub-populations of the upstream energetic ion distribution, primarily delineated by their pitch angles.

The large dark purple regions of near zero ENA flux in all panels of Figure 10a are due to Titan's plasma absorption shadow, formed by the thermalization of particles that reach the MPD. For each production octant, the associated region of the detector sphere lies on the opposite side of the moon from the production octant. For example, production octant I in Figure 10a is centered around  $45^\circ$  latitude and  $45^\circ$  longitude, while the absorption shadow of ENAs from octant I is centered near  $-45^\circ$  latitude and  $225^\circ$  longitude (offset by  $90^\circ$  of latitude and  $180^\circ$  of longitude). ENAs from production octant I, such as ENA in Figure 9b, cannot reach the portion of the detector opposite of the moon. ENA is emitted in the ( $X > 0, Y > 0$ ) sector, but would have to travel through Titan to reach the ( $X < 0, Y < 0$ ) sector. However, the region of the detector diametrically opposed to each production octant is still populated by ENAs from the other octants. More specifically, the portion of the depletion region in the high flux band associated with each production octant is “filled in” by ENAs primarily produced within the same  $Z$  half space. For instance, the dark purple (depleted flux) portion of the equatorial band around  $225^\circ$  longitude in octant I of Figure 10a coincides with the band contributions from octants II, III, and IV. The remaining portion of this dark region which lies “below” the band in octant I is filled in by contributions from all other octants. For each production octant, Titan's absorption of ENAs is therefore replenished by ENAs from other octants in the full ENA map (Figure 5a), and the equatorial high flux band is uninterrupted across all longitudes.

There is a smaller region of depleted ENA flux within the area of the detector directly above each production octant (outlined in red) in Figure 10a. These depletions indicate that the centers of the local detector regions are particularly difficult for parent ions to populate. This difficulty is caused by the limited radial velocity component of detectable ENAs. An energetic parent ion ( $R_g \approx 1.9 R_T$ ) which skims just above the MPD in the course of its gyration will leave the high neutral density of the ENA production shell, which extends only  $\approx 0.3 R_T$  above the MPD, before the radial component of its velocity is large. Therefore it cannot emit ENAs radially outward into the local detector region. Instead, the detector region above each octant is populated by ENAs that have a significant velocity component tangential to the sphere defined by the MPD and that are emitted near the “edges” of the production octant, such as ENA in Figure 9b. This ENA is emitted close to the boundary between octants at

270° longitude. It reaches the outer portion of the local detector region, near 0° longitude. A hypothetical parent ion that could emit an ENA from the same production octant as ENA into the center of the local detector region (near 315° longitude) would be required to travel below the MPD in order to move radially outward within the ENA production shell.

Figure 10b shows the decomposed ENA maps for uniform fields in the  $\vartheta = 30^\circ$  case. Titan's plasma absorption shadow on the opposite side of the moon from each production octant and the depletion in the region local to each production octant are again present. The rotated band of high ENA flux that encircles the moon in Figure 5b, centered where the ambient magnetic field is tangential to the surface, consists of contributions from all octants in Figure 10b. ENAs produced in octants III through VI contribute to the band across all longitudes, indicated by the band's continuous yellow curve in the corresponding panels of Figure 10b. ENAs produced in octants I, II, VII, and VIII contribute significant ENA flux only in the detector regions at longitudes immediately adjacent to the local production region, more similar to the  $\vartheta = 0^\circ$  case in Figure 10a. As in the  $\vartheta = 0^\circ$  case, for  $\vartheta = 30^\circ$  the production octants in the  $Z > 0$  and  $Z < 0$  half spaces contribute more strongly to the upper and lower portions, respectively, of the high flux band.

For  $\vartheta = 30^\circ$ , the high ENA flux band is rotated by the inclined field into the ( $-Z$ ) upstream quadrant and the ( $+Z$ ) downstream quadrant. This rotation translates into an apparent waviness of the band in the two-dimensional projection in Figure 10b. The flux maps in Figure 10b appear highly distinct from those in Figure 10a: octants III through VI now strongly contribute to the high flux band across all longitudes. However, despite the differing appearance of these two sets of decomposed flux maps the mechanisms that produce the global ENA features remain the same. The additional upstream-downstream asymmetry introduced by the field inclination has little impact due to the high velocity of the parent ions ( $\sqrt{2E/m} = 2400$  km/s) compared to the  $\vec{E} \times \vec{B}$  drift velocity ( $V_D = 120$  km/s).

The large difference between the flux maps in Figures 10a and 10b instead arises from the emission pattern being rotated around the  $Y$  axis by the ambient magnetic field inclination angle  $\vartheta = 30^\circ$  while the coordinate system on the detector sphere remains the same as in the  $\vartheta = 0^\circ$  case. Parent ions with pitch angles near  $90^\circ$  that drift near the ( $\pm Z$ ) apices of the production shell play the key role in how this rotation manifests in the decomposed ENA maps. As illustrated by the red gyrocircles in Figure 6, the ENAs emitted by these particles define the “upper” and “lower” edges of the equatorial flux band. Their gyroplanes never intersect the sphere defined by the MPD, allowing them to emit detectable ENAs in all directions without being absorbed. In the  $\vartheta = 0^\circ$  case, these ENAs are generated uniformly within all four production octants intersected by the ion's trajectory. Consequently, these ENAs appear on the detector sphere as two thin longitudinal lines of flux that delineate the “upper” and “lower” boundaries of the high flux band. These lines are visible in Figure 10a: they connect the two larger “patches” of high flux to either side of the respective production region. They can be seen at  $\approx 28^\circ$  latitude in octants I-IV and  $\approx -28^\circ$  latitude in octants V-VIII.

When the ambient magnetic field is inclined, however, the gyroplanes of the ions that produce this feature are rotated around the  $Y$  axis toward the ( $-X, +Z$ ) and ( $+X, -Z$ ) quadrants (see Figure 6b). Due to this geometric change in the location of their gyrocircles, they generate more ENAs within some production octants (III-VI) than within others (octants I, II, VII, and VIII), breaking the symmetry in production from the uninclined case. Consequentially, for  $\vartheta > 0^\circ$  the continuous lines of flux on the detector sphere are stronger for the former group of production octants and weaker for the latter group. Compare, for example, the detected flux at  $225^\circ$  longitude from octants I and V between Figures 10a and 10b. In the  $\vartheta = 0^\circ$  case, the emissions from these two octants are nearly symmetric across the  $Z = 0$  plane, with both displaying the narrow line of elevated flux (light blue) bridging the two brighter features on either side. While in the  $\vartheta = 30^\circ$  case, this bridging feature is largely absent in emissions from octant I and is much stronger (yellow), both in intensity and latitudinal width, in emissions from octant V.

Our results for the uniform field cases already suggest that an ENA detector on a spacecraft may receive high ENA flux that was produced within any portion of the atmosphere unobscured by Titan. In other words, most ENAs are detected non-locally, away from where they are produced.

This non-local detection of ENA emissions remains when field draping is included. The decomposed ENA maps for draped fields in the  $\vartheta = 0^\circ$  and  $30^\circ$  cases are shown in Figures 12a and 12b, respectively. The global reduction in ENA emissions caused by the field perturbations (31% for  $\vartheta = 0^\circ$  and 38% for  $\vartheta = 30^\circ$ ) is evident in all octants

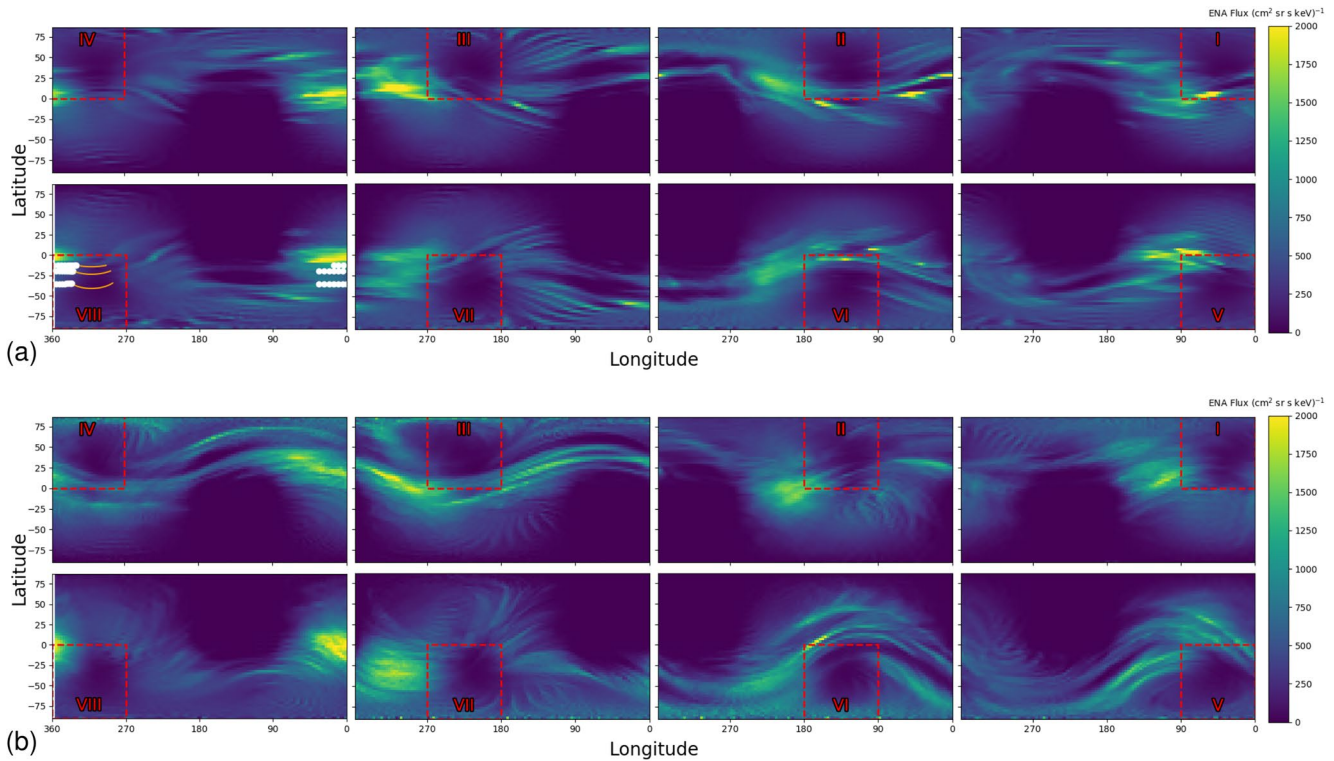


**Figure 12.** (a) Energetic neutral atom (ENA) flux maps for production within eight regions of the atmosphere in the  $\vartheta = 0^\circ$  case for draped fields. The octants are defined and labeled in the same manner as in Figure 10a. The orange lines are the path of the ion trajectory shown in Figure 11b through each production octant, projected radially onto the surface of the detector sphere. The lines are only shown where the parent ion passes within the ENA production shell above the minimum passing distance, that is, they correspond to the green trajectory segments in Figure 11b. This sample ion produces ENAs *only* when traveling through production octant VIII. The white dots indicate where the ENAs emitted by the ion are detected. (b) ENA flux maps for production within eight regions of the atmosphere in the  $\vartheta = 30^\circ$  case for draped fields. The octants are defined and labeled in the same manner as in Figure 10a.

for both field inclinations. The local depletion of ENA flux detected above each production octant (within the red outlined regions) remains in both cases: even within the enhanced fields in the pileup region, parent ions' gyroradii are more than four times larger than the thickness of the ENA production shell (see, e.g., the ion trajectory in the right panels of Figure 11a). An ion which passes just above the MPD as it gyrates is therefore still unable to attain a large radial velocity component before leaving the dense neutral gas within the production shell. Also in the same manner as in uniform fields, Titan's plasma absorption shadow appears in Figures 12a and 12b within the sector of the detector opposite of the moon from each production octant.

For  $\vartheta = 0^\circ$ , the field draping most strongly reduces the ENA flux in the detector regions immediately to the west of each local production octant (outlined in red in Figure 12a). The flux into these detector regions, which contain each octant's strongest contribution to the equatorial flux band and highest emissions in uniform fields, is reduced by  $\approx 25\text{--}50\%$ . This is caused by the deflection of parent ions with pitch angles near  $90^\circ$  that, in uniform fields, would contribute most of the ENAs in the band. For example, in uniform fields (left column) the ion with a solid trajectory in Figure 7b contributes to the elevated flux detected to the west of production octant III. In draped fields (right column, solid trajectory), however, an ion with the same initial conditions is deflected away from Titan and does not produce ENAs at all. For  $\vartheta = 30^\circ$ , the same effect can be seen in the ion trajectory in Figure 7c. This ion produces ENAs in octants IV and VIII in uniform fields, again contributing ENAs to the westward segments of elevated flux due to its sense of gyration. The deflection of the ion in draped fields prevents it from emitting any ENAs and thus reduces emissions into the westward flux segments in Figure 12b that combine to form the high flux band. In production octants III through VI, the deflection of ions with pitch angles near  $90^\circ$  in draped fields reduces ENA emissions into the flux band across all longitudes, as ENAs produced within these octants in uniform fields can contribute to the entire band.

Despite this deflection, some parent ions with pitch angles near  $90^\circ$  are still able to reach Titan and emit significant ENAs. The trajectory of one such particle is shown in Figure 11a for  $\vartheta = 0^\circ$ . This parent ion, like the particles in Figure 7b, has a pitch angle of  $90^\circ$ . All three of these ions are deflected toward ( $-Y$ ) by the field gradient at the ramside of the pileup region. In contrast to the particles from Figure 7b, however, the ion in Figure 11a is able to reach the ENA production shell in octant VIII and emit ENAs (white dots in Figure 12a) mainly perpendicular to the ambient magnetic field. As can be seen from the green segments of the trajectory in Figure 11a, the ion emits ENA flux toward ( $+Y$ ), where it contributes to the equatorial region of elevated flux around  $0^\circ$  longitude of the detector (colored yellow and green) in Figure 12a. As the ion is slightly deflected toward ( $-Z$ ) by the draped fields, the discrete lines of ENAs at increasing latitude (in the ( $-Z$ ) hemisphere) are formed by the portions of three gyrations that intersect the ENA production shell (orange lines in Figure 12a). Due to particles such as this one, the ENA flux into the detector regions west of each production octant remains up to twice as high as the “background” ENA flux (depicted in light blue) emitted into much of the rest of the detector sphere, for all octants and for draped fields with  $\vartheta = 0^\circ$  and  $\vartheta = 30^\circ$  (Figures 12a and 12b).

The “background” ENA flux that reaches much of the remainder of the detector sphere is mainly produced by those parent ions that spiral toward Titan with large field-aligned velocity components. The highest emissions of these parent ions in uniform fields are detected to either side of each production octant (see Figures 10a and 10b) due to the parent ions' ability to gyrate around Titan and produce ENAs during any portion of their gyromotion. For instance, the parent ion shown in the left panels of Figure 11b encircles the MPD and contributes to this eastward region in uniform fields for  $\vartheta = 30^\circ$ . Its trajectory through the ENA production shell is indicated by the orange lines and its ENA emissions by the white dots in Figure 10b. In draped fields of both inclinations  $\vartheta$  (Figures 12a and 12b), however, the emissions detected to the east of the production octants are similar in intensity to the surrounding “background” emissions (Figures 10a and 10b). The reason for this is illustrated in the right panels of Figure 11b. In this case, a parent ion launched with the same initial conditions in draped fields is decelerated and reflected away from Titan by the high-latitude pileup region before it reaches the ENA production shell. The enhanced flux detected to the east of each production octant in uniform fields (Figure 10b), being emitted by ions such as that in Figure 11b, is thus strongly attenuated by the field perturbations.

However, some parent ions with helical trajectories such as that shown in Figure 7a may instead have their ENA emissions enhanced by the field draping. Such ions generate the localized yellow “spots” of elevated flux originating from, for example, production octants II and VI for  $\vartheta = 0^\circ$  (Figure 12a) and contribute to the (attenuated) flux band. For example, the ENA-emitting segments (colored green) of the ion trajectory in the right panels of Figure 7a intersect all four production octants in Titan's ( $+Y$ ) hemisphere (octants I, IV, V, and VIII). The tangents of these segments point into the ( $+Y$ ) hemisphere of the detector, such that the ENAs emitted by this ion contribute to the elevated flux from around  $340^\circ$ – $45^\circ$  longitude (colored yellow) for those octants in Figure 12a. The ion's velocity is mainly perpendicular to the magnetic field while it travels through the production shell, so the ENAs it emits are detected near the equator.

#### 4. Summary and Concluding Remarks

In this study we have modeled Titan's global ENA emission morphology under different upstream conditions produced by the moon's varying location with respect to the center of Saturn's magnetodisk current sheet. In particular, we examined the ENA emissions for three sweepback angles of the upstream magnetic field, representative of Titan both within and away from the center of the sheet. We set out to determine the influence of the field pileup and draping in the moon's induced magnetosphere on global ENA emissions. As Cassini typically captured ENA images at altitudes of several Titan radii, the ENAs traveled some distance before being detected. Their origin with respect to the spacecraft determines whether the dynamics of the associated parent ions were influenced by local or remote field structures. We therefore further intended to assess the locality of ENA detections to their generation. Our goal was to study the ENA emission morphology holistically, without artificial truncation of any ENAs by our choice of detector viewing geometry.

To model ENA emissions at Titan, we used the AIKEF hybrid (kinetic ions, fluid electrons) model to determine the electromagnetic fields in the moon's interaction region under three inclinations of the upstream magnetic field against the corotation direction:  $90^\circ$  (i.e.,  $\vec{u}_0 \perp \vec{B}_0$ ),  $60^\circ$ , and  $30^\circ$  (corresponding to  $\vartheta = 0^\circ$ ,  $30^\circ$ , and  $60^\circ$  in Equation 1). We treated the energetic ion population as test particles and used a separate tracing code to determine the trajectories of over 1.1 billion energetic protons in the draped fields produced by AIKEF. Our approach

takes into account that the energetic ions' field-aligned velocity components can greatly exceed the  $\vec{E} \times \vec{B}$  drift velocity, that is, for  $\vartheta \neq 0^\circ$  a portion of the incident ion population approaches Titan from downstream. In our model, parent ions that travel through the atmosphere (which is treated as a continuum) emit ENAs along tangents of their curved trajectories. The ENAs are propagated along straight line paths into a spherical detector (with radius  $3 R_T$ ) concentric with the moon that fully encompasses the ENA production region in our model. We also decomposed the ENA production region into sectors and assessed the (angular) deviations between the locations of ENA production and detection.

Our major findings are as follows:

1. Titan's detectable ENA emissions are strongest within a band of flux that encircles the moon perpendicular to the ambient magnetospheric field. The ENAs in this flux band are primarily produced by parent ions with pitch angles near  $90^\circ$ . As a result, the latitudinal half-width of the band is moderated by the radial atmospheric density profile. Due to the decreasing neutral density with altitude, nearly all ENA production occurs below 1,800 km altitude. Additionally, a peak in production forms around 1,400 km due to the neutralization of most parent ions before they penetrate deeper into the atmosphere. These constraints on the radial extension of the ENA production region and the peak flux altitude are in agreement with Cassini INCA observations (Smith et al., 2009). The inclined magnetospheric field tilts the parent ion gyroplanes, resulting in a rotation of the flux band around an axis perpendicular to the ambient field and corotation direction.
2. The field line draping in Titan's induced magnetosphere lowers the intensity of ENA emissions through the spherical detector. However, it does not change the overall morphology of the emission pattern, that is, the highest fluxes are still confined to a band around the moon, but are about three times weaker compared to in uniform fields. This attenuation is mainly caused by the magnetic enhancement in the ramside pileup region partially shielding the atmosphere from parent ions with pitch angles near  $90^\circ$ . When the ambient field has a component along the corotation direction, the ramside field enhancement is weakened and the pileup region is displaced southward and partially dragged downstream by the corotational flow. The weaker pileup fields are less able to deflect parent ions away from Titan, so the intensity of the ENA emissions increases with the ambient field inclination. In other words, our results suggest that the intensity of Titan's ENA emissions increases when the center of Saturn's oscillating magnetodisk current sheet moves away from Titan's orbital plane. The ENAs' high sensitivity to the field perturbations is in agreement with observed variability in ENA flux between Cassini flybys (Garnier et al., 2010).
3. Using plane detectors, which place limits on the detectable ENA emissions in both position and velocity space, both Wulms et al. (2010) and Kabanovic et al. (2018) found strong effects of the field draping on the ENA emission morphology. These include shifts in regions of maximum and minimum flux, the appearance and disappearance of regions containing zero flux, and both localized increases and decreases in the flux intensity. In their models, the influence of the draping varies with the location of the plane detector, from very little impact to a complete mirroring of the flux pattern. These effects seem to stem from the restriction of detectable ENA trajectories to those nearly normal to the modeled detector, that is, each of their synthetic ENA images is based upon only a small portion of the ENA population. We find that the field draping does not introduce such strong changes in the ENA emissions through a spherical global detector, which captures all emitted ENAs. When we partition the detected ENAs based on where they are produced, we find that the field draping more strongly attenuates ENA emission into some directions than others. This directional asymmetry in our detected flux is consistent with the viewing direction dependence in the results of both previous studies. Using the fields from a hybrid model, we find that the field draping has a weaker impact on the ENA morphology than seen in the fields from an MHD code (Wulms et al., 2010). For instance, we do not see a reversal of the hemisphere containing maximum flux. Kabanovic et al. (2018) demonstrate that this discrepancy is due to the weaker pileup in the hybrid model compared to the MHD model.
4. The large majority of ENAs leave Titan's atmosphere non-locally, that is, they may be detected far from where they were produced. Most ENAs emitted into the high flux band reach our spherical detector around  $90^\circ$  of longitude west of where they are generated due to the sense of the parent ions' gyration. Few ENAs are detected directly "above" their production region, as the parent ions' large gyroradii lead them to be thermalized in the dense low-altitude atmosphere before they can emit ENAs radially outward. Even ENA observations made by a spacecraft directly above Titan's atmosphere therefore probe remote field structures rather than local ones.

5. In draped magnetic fields, some parent ions travel along particularly complex trajectories. For instance, ions with significant field-aligned velocity components may be reflected by a magnetic mirror force as they reach the “edges” of the pileup region. When the ambient field has a component along the corotation direction, some of these ions are reflected by the downstream portion of the pileup region *after* passing through the atmosphere. These particles may not escape Titan as ENAs until they reenter the atmosphere and are neutralized on their way back upstream.

Because most ENAs are detected non-locally to where they are produced, multiple ENA images taken under identical upstream plasma, magnetospheric field, and atmospheric conditions from multiple vantage points are required to unambiguously link ENA emission features to electromagnetic field signatures. The high magnetospheric variability along Titan's orbit makes this impossible to realize, however, as each spacecraft flyby occurs under different ambient conditions and images different field draping signatures. This even holds for flybys that occur at the same local time (Simon et al., 2010b). An approach to ENA analysis that requires consistent upstream conditions between different flybys is better suited at Europa or Ganymede, where nearly the same field conditions occur during every synodic rotation (e.g., Addison et al., 2021).

### Data Availability Statement

Results from both the AIKEF hybrid model and the particle tracing model can be downloaded at <https://doi.org/10.5281/zenodo.6603948>.

### Acknowledgments

The authors are grateful to NASA's Cassini Data Analysis Program (2017, Grant 80NSSC18K0968, and 2022) and Solar System Workings Program (Grant 80NSSC22K0097) for financial support. The authors are also grateful to both referees for careful inspection of the manuscript and for valuable comments.

### References

- Ågren, K., Wahlund, J.-E., Garnier, P., Modolo, R., Cui, J., Galand, M., & Muller-Wodarg, I. (2009). On the ionospheric structure of Titan. *Planetary and Space Science*, 57(14), 1821–1827. <https://doi.org/10.1016/j.pss.2009.04.012>
- Achilleos, N., Arridge, C. S., Bertucci, C., Guio, P., Romanelli, N., & Sergis, N. (2014). A combined model of pressure variations in Titan's plasma environment. *Geophysical Research Letters*, 41(24), 8730–8735. <https://doi.org/10.1002/2014GL061747>
- Addison, P., Liuzzo, L., Arnold, H., & Simon, S. (2021). Influence of Europa's time-varying electromagnetic environment on magnetospheric ion precipitation and surface weathering. *Journal of Geophysical Research: Space Physics*, 126(5), e2020JA029087. <https://doi.org/10.1029/2020JA029087>
- Amsif, A., Dandouras, J., & Roelof, E. C. (1997). Modelling the production and the imaging of energetic neutral atoms from Titan's exosphere. *Journal of Geophysical Research*, 102(A10), 22169–22181. <https://doi.org/10.1029/97ja01597>
- Arridge, C. S., Achilleos, N., & Guio, P. (2011). Electric field variability and classifications of Titan's magnetoplasma environment. *Annales Geophysicae*, 29(7), 1253–1258. <https://doi.org/10.5194/angeo-29-1253-2011>
- Arridge, C. S., André, N., Bertucci, C. L., Garnier, P., Jackman, C. M., Németh, Z., et al. (2011). Upstream of Saturn and Titan. *Space Science Reviews*, 162(1–4), 25–83. <https://doi.org/10.1007/s11214-011-9849-x>
- Arridge, C. S., Khurana, K. K., Russell, C. T., Southwood, D. J., Achilleos, N., Dougherty, M. K., et al. (2008). Warping of Saturn's magnetospheric and magnetotail current sheets. *Journal of Geophysical Research*, 113(A12), A08217. <https://doi.org/10.1029/2007JA012963>
- Arridge, C. S., Russell, C. T., Khurana, K. K., Achilleos, N., André, N., Rymer, A. M., et al. (2007). Mass of Saturn's magnetodisc: Cassini observations. *Geophysical Research Letters*, 34(9), L09108. <https://doi.org/10.1029/2006GL028921>
- Arridge, C. S., Russell, C. T., Khurana, K. K., Achilleos, N., Cowley, S. W. H., Dougherty, M. K., et al. (2008). Saturn's magnetodisc current sheet. *Journal of Geophysical Research*, 113(A12), A04214. <https://doi.org/10.1029/2007JA012540>
- Backes, H., Neubauer, F. M., Dougherty, M. K., Achilleos, N., André, N., Arridge, C. S., et al. (2005). Titan's magnetic field signature during the first Cassini encounter. *Science*, 308(5724), 992–995. <https://doi.org/10.1126/science.1109763>
- Bagenal, F., & Delamere, P. A. (2011). Flow of mass and energy in the magnetospheres of Jupiter and Saturn. *Journal of Geophysical Research*, 116(A5), A05209. <https://doi.org/10.1029/2010JA016294>
- Bertucci, C. (2009). Characteristics and variability of Titan's magnetic environment. *Royal Society of London Philosophical Transactions Series A*, 367(1889), 789–798. <https://doi.org/10.1098/rsta.2008.0250>
- Bertucci, C., Achilleos, N., Dougherty, M. K., Modolo, R., Coates, A. J., Szego, K., et al. (2008). The magnetic memory of Titan's ionized atmosphere. *Science*, 321(5895), 1475–1478. <https://doi.org/10.1126/science.1159780>
- Bertucci, C., Hamilton, D. C., Kurth, W. S., Hospodarsky, G., Mitchell, D., Sergis, N., et al. (2015). Titan's interaction with the supersonic solar wind. *Geophysical Research Letters*, 42(2), 193–200. <https://doi.org/10.1002/2014GL062106>
- Bertucci, C., Sinclair, B., Achilleos, N., Hunt, P., Dougherty, M. K., & Arridge, C. S. (2009). The variability of Titan's magnetic environment. *Planetary and Space Science*, 57(14–15), 1813–1820. <https://doi.org/10.1016/j.pss.2009.02.009>
- Brandt, P., Dialynas, K., Dandouras, I., Mitchell, D., Garnier, P., & Krimigis, S. (2012). The distribution of Titan's high-altitude (out to ~50,000 km) exosphere from energetic neutral atom (ENA) measurements by Cassini/INCA. *Planetary and Space Science*, 60(1), 107–114. <https://doi.org/10.1016/j.pss.2011.04.014>
- Carbary, J. F., & Mitchell, D. G. (2016). Seasonal variations in Saturn's plasma sheet warping. *Geophysical Research Letters*, 43(23), 11957–11962. <https://doi.org/10.1002/2016GL071790>
- Chen, C., & Simon, S. (2020). A comprehensive study of Titan's magnetic pile-up region during the Cassini era. *Planetary and Space Science*, 191, 105037. <https://doi.org/10.1016/j.pss.2020.105037>
- Coates, A. J. (2009). Interaction of Titan's ionosphere with Saturn's magnetosphere. *Philosophical Transactions of the Royal Society A: Mathematical, Physical & Engineering Sciences*, 367(1889), 773–788. <https://doi.org/10.1098/rsta.2008.0248>
- Coates, A. J., Wahlund, J. E., Ågren, K., Edberg, N., Cui, J., Wellbrock, A., & Szego, K. (2011). Recent results from Titan's ionosphere. *Space Science Reviews*, 162(1–4), 85–111. <https://doi.org/10.1007/s11214-011-9826-4>

- Cowee, M. M., Gary, S. P., Wei, H. Y., Tokar, R. L., & Russell, C. T. (2010). An explanation for the lack of ion cyclotron wave generation by pickup ions at Titan: 1-D hybrid simulation results. *Journal of Geophysical Research*, *115*(A10). <https://doi.org/10.1029/2010JA015769>
- Cui, J., Yelle, R. V., Vuitton, V., Waite, J. H., Kasprzak, W. T., Gell, D. A., et al. (2009). Analysis of Titan's neutral upper atmosphere from Cassini ion neutral mass spectrometer measurements. *Icarus*, *200*(2), 581–615. <https://doi.org/10.1016/j.icarus.2008.12.005>
- Dandouras, J., & Amsif, A. (1999). Production and imaging of energetic neutral atoms from Titan's exosphere: A 3-D model. *Planetary and Space Science*, *47*(10–11), 1355–1369. [https://doi.org/10.1016/S0032-0633\(99\)00057-4](https://doi.org/10.1016/S0032-0633(99)00057-4)
- Dialynas, K., Brandt, P. C., Krimigis, S. M., Mitchell, D. G., Hamilton, D. C., Krupp, N., & Rymer, A. M. (2013). The extended Saturnian neutral cloud as revealed by global ENA simulations using Cassini/MIMI measurements. *Journal of Geophysical Research: Space Physics*, *118*(6), 3027–3041. <https://doi.org/10.1002/jgra.50295>
- Dialynas, K., Krimigis, S. M., Mitchell, D. G., Hamilton, D. C., Krupp, N., & Brandt, P. C. (2009). Energetic ion spectral characteristics in the Saturnian magnetosphere using Cassini/MIMI measurements. *Journal of Geophysical Research*, *114*(A1), A01212. <https://doi.org/10.1029/2008JA013761>
- Dialynas, K., Roussos, E., Regoli, L., Paranicas, C. P., Krimigis, S. M., Kane, M., et al. (2018). Energetic ion moments and polytropic index in Saturn's magnetosphere using Cassini/MIMI measurements: A simple model based on  $\kappa$ -distribution functions. *Journal of Geophysical Research: Space Physics*, *123*(10), 8066–8086. <https://doi.org/10.1029/2018JA025820>
- Dougherty, M. K., Cao, H., Khurana, K. K., Hunt, G. J., Provan, G., Kellock, S., et al. (2018). Saturn's magnetic field revealed by the Cassini Grand Finale. *Science*, *362*(6410), eaat5434. <https://doi.org/10.1126/science.aat5434>
- Edberg, N. J. T., Andrews, D. J., Shebanits, O., Ågren, K., Wahlund, J.-E., Opgenoorth, H. J., et al. (2013). Extreme densities in Titan's ionosphere during the T85 magnetosheath encounter. *Geophysical Research Letters*, *40*(12), 2879–2883. <https://doi.org/10.1002/grl.50579>
- Feyerabend, M., Simon, S., Motschmann, U., & Liuzzo, L. (2015). Filamented ion tail structures at Titan: A hybrid simulation study. *Planetary and Space Science*, *117*, 362–376. <https://doi.org/10.1016/j.pss.2015.07.008>
- Feyerabend, M., Simon, S., Neubauer, F. M., Motschmann, U., Bertucci, C., Edberg, N. J. T., et al. (2016). Hybrid simulation of Titan's interaction with the supersonic solar wind during Cassini's T96 flyby. *Geophysical Research Letters*, *43*(1), 35–42. <https://doi.org/10.1002/2015GL066848>
- Garnier, P., Dandouras, I., Toublanc, D., Roelof, E. C., Brandt, P. C., Mitchell, D. G., et al. (2008). The lower exosphere of Titan: Energetic neutral atoms absorption and imaging. *Journal of Geophysical Research*, *113*(A12), A10216. <https://doi.org/10.1029/2008JA013029>
- Garnier, P., Dandouras, I., Toublanc, D., Roelof, E. C., Brandt, P. C., Mitchell, D. G., et al. (2010). Statistical analysis of the energetic ion and ENA data for the Titan environment. *Planetary and Space Science*, *58*(14–15), 1811–1822. <https://doi.org/10.1016/j.pss.2010.08.009>
- Gombosi, T. I., Armstrong, T. P., Arridge, C. S., Khurana, K. K., Krimigis, S. M., Krupp, N., et al. (2009). Saturn's magnetospheric configuration. In M. K. Dougherty, L. W. Esposito, & S. M. Krimigis (Eds.), *Saturn from Cassini-Huygens* (pp. 203–255). Springer Netherlands.
- Hartle, R. E., Sittler, E. C., Neubauer, F. M., Johnson, R. E., Smith, H. T., Cray, F., et al. (2006). Preliminary interpretation of Titan plasma interaction as observed by the Cassini plasma spectrometer: Comparisons with Voyager 1. *Geophysical Research Letters*, *33*(8), L08201. <https://doi.org/10.1029/2005GL024817>
- Hill, T. W. (1979). Inertial limit on corotation. *Journal of Geophysical Research*, *84*(A11), 6554–6558. <https://doi.org/10.1029/JA084A11p06554>
- Janev, R. K., & Reiter, D. (2002). Collision processes of CH<sub>3</sub> and CH<sub>3</sub><sup>+</sup> hydrocarbons with plasma electrons and protons. *Physics of Plasmas*, *9*(9), 4071–4081. <https://doi.org/10.1063/1.1500735>
- Johnson, L. K., Gao, R. S., Smith, K. A., & Stebbings, R. F. (1988). Absolute differential cross sections for very-small-angle scattering of keV H and He atoms by H<sub>2</sub> and N<sub>2</sub>. *Physical Review A*, *38*(6), 2794–2797. <https://doi.org/10.1103/PhysRevA.38.2794>
- Kabanovic, S., Feyerabend, M., Simon, S., Meeks, Z., & Wulms, V. (2018). Influence of asymmetries in the magnetic draping pattern at Titan on the emission of energetic neutral atoms. *Planetary and Space Science*, *152*, 142–164. <https://doi.org/10.1016/j.pss.2017.12.017>
- Kabanovic, S., Simon, S., Neubauer, F. M., & Meeks, Z. (2017). An empirical model of Titan's magnetic environment during the Cassini era: Evidence for seasonal variability. *Journal of Geophysical Research: Space Physics*, *122*(11), 11076–11085. <https://doi.org/10.1002/2017JA024402>
- Kallio, E., Sillanpää, I., Jarvinen, R., Janhunen, P., Dougherty, M., Bertucci, C., & Neubauer, F. (2007). Morphology of the magnetic field near Titan: Hybrid model study of the Cassini T9 flyby. *Geophysical Research Letters*, *34*(24), L24S09. <https://doi.org/10.1029/2007GL030827>
- Kane, M., Mitchell, D. G., Carbary, J. F., Dialynas, K., Hill, M. E., & Krimigis, S. M. (2020). Convection in the magnetosphere of Saturn during the Cassini mission derived from MIMI INCA and CHEMS measurements. *Journal of Geophysical Research: Space Physics*, *125*(2), e2019JA027534. <https://doi.org/10.1029/2019JA027534>
- Khurana, K. K., Mitchell, D. G., Arridge, C. S., Dougherty, M. K., Russell, C. T., Paranicas, C., et al. (2009). Sources of rotational signals in Saturn's magnetosphere. *Journal of Geophysical Research*, *114*(A2), A02211. <https://doi.org/10.1029/2008JA013312>
- Khurana, K. K., Russell, C., & Dougherty, M. (2008). Magnetic portraits of Tethys and Rhea. *Icarus*, *193*(2), 465–474. <https://doi.org/10.1016/j.icarus.2007.08.005>
- Krimigis, S. M., Mitchell, D. G., Hamilton, D. C., Krupp, N., Livi, S., Roelof, E. C., et al. (2005). Dynamics of Saturn's magnetosphere from MIMI during Cassini's orbital insertion. *Science*, *307*(5713), 1270–1273. <https://doi.org/10.1126/science.1105978>
- Krimigis, S. M., Mitchell, D. G., Hamilton, D. C., Livi, S., Dandouras, J., Jaskulek, S., et al. (2004). Magnetosphere imaging instrument (MIMI) on the Cassini mission to Saturn/Titan. *Space Science Reviews*, *114*(1–4), 233–329. <https://doi.org/10.1007/s11214-004-1410-8>
- Ledvina, S. A., Brecht, S. H., & Cravens, T. E. (2012). The orientation of Titan's dayside ionosphere and its effects on Titan's plasma interaction. *Earth Planets and Space*, *64*(2), 207–230. <https://doi.org/10.5047/eps.2011.08.009>
- Lindsay, B. G., & Stebbings, R. F. (2005). Charge transfer cross sections for energetic neutral atom data analysis. *Journal of Geophysical Research*, *110*(A12), A12213. <https://doi.org/10.1029/2005JA011298>
- Luhmann, J. G. (1996). Titan's ion exosphere wake: A natural ion mass spectrometer? *Journal of Geophysical Research*, *101*(E12), 29387–29393. <https://doi.org/10.1029/96JE03307>
- Ma, Y. J., Nagy, A. F., Cravens, T. E., Sokolov, I. V., Hansen, K. C., Wahlund, J.-E., et al. (2006). Comparisons between MHD model calculations and observations of Cassini flybys of Titan. *Journal of Geophysical Research*, *111*(A5), A05207. <https://doi.org/10.1029/2005JA011481>
- Mitchell, D. G., Brandt, P. C., Roelof, E. C., Dandouras, J., Krimigis, S. M., & Mauk, B. H. (2005). Energetic neutral atom emissions from Titan interaction with Saturn's magnetosphere. *Science*, *308*(5724), 989–992. <https://doi.org/10.1126/science.1109805>
- Mitchell, D. G., Cheng, A. F., Krimigis, S. M., Keath, E. P., Jaskulek, S. E., Mauk, B. H., et al. (1993). INCA: The ion neutral camera for energetic neutral atom imaging of the Saturnian magnetosphere. *Optical Engineering*, *32*(12), 3096–3101. <https://doi.org/10.1117/12.155609>
- Modolo, R., & Chantaur, G. M. (2008). A global hybrid model for Titan's interaction with the Kronian plasma: Application to the Cassini Ta flyby. *Journal of Geophysical Research*, *113*(A12), A01317. <https://doi.org/10.1029/2007JA012453>
- Modolo, R., Chantaur, G. M., Wahlund, J.-E., Canu, P., Kurth, W. S., Gurnett, D., et al. (2007). Plasma environment in the wake of Titan from hybrid simulation: A case study. *Geophysical Research Letters*, *34*(24), L24S07. <https://doi.org/10.1029/2007GL030489>
- Müller, J., Simon, S., Motschmann, U., Schüle, J., Glassmeier, K.-H., & Pringle, G. J. (2011). A.I.K.E.F.: Adaptive hybrid model for space plasma simulations. *Computer Physics Communications*, *182*(4), 946–966. <https://doi.org/10.1016/j.cpc.2010.12.033>

- Muller-Wodarg, I., Griffith, C., Lellouch, E., & Cravens, T. (Eds.). (2014). *Titan: Interior, surface, atmosphere, and space environment*. Cambridge University Press. <https://doi.org/10.1017/CBO9780511667398>
- Muller-Wodarg, I. C. F., Yelle, R. V., Cui, J., & Waite, J. H. (2008). Horizontal structures and dynamics of Titan's thermosphere. *Journal of Geophysical Research*, *113*(E10), E10005. <https://doi.org/10.1029/2007JE003033>
- Neubauer, F. M. (1980). Nonlinear standing Alfvén wave current system at Io: Theory. *Journal of Geophysical Research*, *85*(A3), 1171–1178. <https://doi.org/10.1029/JA085iA03p01171>
- Neubauer, F. M., Backes, H., Dougherty, M. K., Wennmacher, A., Russell, C. T., Coates, A., et al. (2006). Titan's near magnetotail from magnetic field and plasma observations and modelling: Cassini flybys TA, TB and T3. *Journal of Geophysical Research*, *111*(A10), A10220. <https://doi.org/10.1029/2006JA011676>
- Neubauer, F. M., Gurnett, D. A., Scudder, J. D., & Hartle, R. E. (1984). Titan's magnetospheric interaction. In T. Gehrels & M. S. Matthews (Eds.), *Saturn* (pp. 760–787). University of Arizona Press.
- Persoon, A. M., Gurnett, D. A., Santolik, O., Kurth, W. S., Faden, J. B., Groene, J. B., et al. (2009). A diffusive equilibrium model for the plasma density in Saturn's magnetosphere. *Journal of Geophysical Research*, *114*(A4), A04211. <https://doi.org/10.1029/2008JA013912>
- Regoli, L. H., Roussos, E., Dialynas, K., Luhmann, J. G., Sergis, N., Jia, X., et al. (2018). Statistical study of the energetic proton environment at Titan's orbit from the Cassini spacecraft. *Journal of Geophysical Research: Space Physics*, *123*(6), 4820–4834. <https://doi.org/10.1029/2018JA025442>
- Regoli, L. H., Roussos, E., Feyerabend, M., Jones, G. H., Krupp, N., Coates, A. J., et al. (2016). Access of energetic particles to Titan's exobase: A study of Cassini's T9 flyby. *Planetary and Space Science*, *130*, 40–53. <https://doi.org/10.1016/j.pss.2015.11.013>
- Richards, P. C., Fennelly, J. A., & Torr, D. G. (1994). EUVAC: A solar EUV flux model for aeronomic calculations. *Journal of Geophysical Research*, *99*(A5), 8981–8992. <https://doi.org/10.1029/94ja00518>
- Richardson, J. D. (1998). Thermal plasma and neutral gas in Saturn's magnetosphere. *Reviews of Geophysics*, *36*(4), 501–524. <https://doi.org/10.1029/98RG01691>
- Roederer, J. G. (1967). On the adiabatic motion of energetic particles in a model magnetosphere. *Journal of Geophysical Research*, *72*(3), 981–992. <https://doi.org/10.1029/JZ072i003p00981>
- Sergis, N., Jackman, C. M., Thomsen, M. F., Krimigis, S. M., Mitchell, D. G., Hamilton, D. C., et al. (2017). Radial and local time structure of the Saturnian ring current, revealed by Cassini. *Journal of Geophysical Research: Space Physics*, *122*(2), 1803–1815. <https://doi.org/10.1002/2016JA023742>
- Simon, S., Addison, P., & Liuzzo, L. (2022). formation of a displaced plasma wake at Neptune's moon Triton. *Journal of Geophysical Research: Space Physics*, *127*(1), e2021JA029958. <https://doi.org/10.1029/2021JA029958>
- Simon, S., Boesswetter, A., Bagdonat, T., Motschmann, U., & Glassmeier, K.-H. (2006). Plasma environment of Titan: A 3-D hybrid simulation study. *Annals of Geophysics*, *24*(3), 1113–1135. <https://doi.org/10.5194/angeo-24-1113-2006>
- Simon, S., Boesswetter, A., Bagdonat, T., Motschmann, U., & Schuele, J. (2007). Three-dimensional multispecies hybrid simulation of Titan's highly variable plasma environment. *Annales Geophysicae*, *25*(1), 117–144. <https://doi.org/10.5194/angeo.25.117.2007>
- Simon, S., Kleindienst, G., Boesswetter, A., Bagdonat, T., Motschmann, U., Glassmeier, K.-H., et al. (2007). Hybrid simulation of Titan's magnetic field signature during the Cassini T9 flyby. *Geophysical Research Letters*, *34*(24), L24S08. <https://doi.org/10.1029/2007GL029967>
- Simon, S., & Motschmann, U. (2009). Titan's induced magnetosphere under non-ideal upstream conditions: 3D multi-species hybrid simulations. *Planetary and Space Science*, *57*(14–15), 2001–2015. <https://doi.org/10.1016/j.pss.2009.08.010>
- Simon, S., Motschmann, U., Kleindienst, G., Glassmeier, K.-H., Bertucci, C., & Dougherty, M. K. (2008). Titan's magnetic field signature during the Cassini T34 flyby: Comparison between hybrid simulations and MAG data. *Geophysical Research Letters*, *35*(4), L04107. <https://doi.org/10.1029/2007GL033056>
- Simon, S., Roussos, E., & Paty, C. S. (2015). The interaction between Saturn's moons and their plasma environments. *Physics Reports*, *602*, 1–65. <https://doi.org/10.1016/j.physrep.2015.09.005>
- Simon, S., van Treeck, S. C., Wennmacher, A., Saur, J., Neubauer, F. M., Bertucci, C. L., & Dougherty, M. K. (2013). Structure of Titan's induced magnetosphere under varying background magnetic field conditions: Survey of Cassini magnetometer data from flybys TA-T85. *Journal of Geophysical Research: Space Physics*, *118*(4), 1679–1699. <https://doi.org/10.1002/jgra.50096>
- Simon, S., Wennmacher, A., Neubauer, F., Bertucci, C., Kriegel, H., Saur, J., & Dougherty, M. K. (2010a). Dynamics of Saturn's magnetodisk near Titan's orbit: Comparison of Cassini magnetometer observations from real and virtual Titan flybys. *Planetary and Space Science*, *58*(12), 1625–1635. <https://doi.org/10.1016/j.pss.2010.08.006>
- Simon, S., Wennmacher, A., Neubauer, F., Bertucci, C., Kriegel, H., Saur, J., et al. (2010b). Titan's highly dynamic magnetic environment: A systematic survey of Cassini magnetometer observations from flybys TA–T62. *Planetary and Space Science*, *58*(10), 1230–1251. <https://doi.org/10.1016/j.pss.2010.04.021>
- Sittler, E. C., Hartle, R. E., Johnson, R. E., Cooper, J. F., Lipatov, A. S., Bertucci, C., et al. (2010). Saturn's magnetospheric interaction with Titan as defined by Cassini encounters T9 and T18: New results. *Planetary and Space Science*, *58*(3), 327–350. <https://doi.org/10.1016/j.pss.2009.09.017>
- Smith, H., Mitchell, D., Johnson, R., & Paranicas, C. (2009). Investigation of energetic proton penetration in Titan's atmosphere using the Cassini INCA instrument. *Planetary and Space Science*, *57*(13), 1538–1546. <https://doi.org/10.1016/j.pss.2009.03.013>
- Snowden, D., & Higgins, A. (2021). A Monte Carlo model of energy deposition, ionization, and sputtering due to thermal ion precipitation into Titan's upper atmosphere. *Icarus*, *354*, 113929. <https://doi.org/10.1016/j.icarus.2020.113929>
- Snowden, D., Smith, M., Jimson, T., & Higgins, A. (2018). Energy deposition and ion production from thermal oxygen ion precipitation during Cassini's T57 flyby. *Icarus*, *305*, 186–197. <https://doi.org/10.1016/j.icarus.2018.01.014>
- Snowden, D., & Yelle, R. (2014). The thermal structure of Titan's upper atmosphere, II: Energetics. *Icarus*, *228*, 64–77. <https://doi.org/10.1016/j.icarus.2013.08.027>
- Teolis, B. D., Niemann, H. B., Waite, J. H., Gell, D. A., Perryman, R. S., Kasprzak, W. T., et al. (2015). A revised sensitivity model for Cassini INMS: Results at Titan. *Space Science Reviews*, *190*(1), 47–84. <https://doi.org/10.1007/s11214-014-0133-8>
- Thomsen, M. F., Reisenfeld, D. B., Delapp, D. M., Tokar, R. L., Young, D. T., Cray, F. J., et al. (2010). Survey of ion plasma parameters in Saturn's magnetosphere. *Journal of Geophysical Research*, *115*(A10), A10220. <https://doi.org/10.1029/2010JA015267>
- Wahlund, J.-E., Boström, R., Gustafsson, G., Gurnett, D. A., Kurth, W. S., Pedersen, A., et al. (2005). Cassini measurements of cold plasma in the ionosphere of Titan. *Science*, *308*(5724), 986–989. <https://doi.org/10.1126/science.1109807>

- Wei, H. Y., Russell, C. T., Wellbrock, A., Dougherty, M. K., & Coates, A. J. (2009). Plasma environment at Titan's orbit with Titan present and absent. *Geophysical Research Letters*, *36*(23), L23202. <https://doi.org/10.1029/2009GL041048>
- Westlake, J. H., Bell, J. M., Waite, J. H., Jr., Johnson, R. E., Luhmann, J. G., Mandt, K. E., et al. (2011). Titan's thermospheric response to various plasma environments. *Journal of Geophysical Research*, *116*(A3), A03318. <https://doi.org/10.1029/2010JA016251>
- Wulms, V., Saur, J., Strobel, D. F., Simon, S., & Mitchell, D. G. (2010). Energetic neutral atoms from Titan: Particle simulations in draped magnetic and electric fields. *Journal of Geophysical Research*, *115*(A14), A06310. <https://doi.org/10.1029/2009JA014893>